INVESTIGATING THREE-DIMENSIONAL (3D) EVOLUTION OF SUBMARINE LANDSLIDE INITIATION AND DYNAMICS

Manuscript submitted to Journal of Geophysical Research: Earth Surface on 18/11/2021;
revised version submitted on 09/02/2022

Wangcheng Zhang
Assistant professor
Department of Engineering
Durham University
South Road, Durham, DH1 3LE, UK
Email: wangcheng.zhang@durham.ac.uk

Formerly
Institute for Geotechnical Engineering, ETH Zurich
Stefano Franscini Platz 5, 8093 Zurich, Switzerland
Email: wangcheng.zhang@igt.baug.ethz.ch

Alexander M. Puzrin
Professor
Institute for Geotechnical Engineering, ETH Zurich
Stefano Franscini Platz 5, 8093 Zurich, Switzerland
Email: alexander.puzrin@igt.baug.ethz.ch

No of words (excluding abstract, acknowledgements, appendix and references): 7757
No of figures: 19
No of tables: 3

Investigating three-dimensional (3D) evolution of submarine landslide initiation and dynamics

ABSTRACT

Submarine landslides are usually enormous in size but often developed from a minute slip surface. Attention has previously been paid to quantifying the failure initiation of a submarine landslide through two-dimensional (2D) plane strain slope stability analyses. The findings of failure initiation from the 2D simplifications need to be justified in a realistic 3D scenario, and more importantly, are inconvenient to apply into analysing the subsequent 3D post-failure behaviours. This study aims to explore to discover the true physical mechanism of submarine landslides and to establish practical criteria for submarine slope stability analysis, by modelling and investigating the whole 3D landslide evolution integrating both the failure initiation and post-failure behaviours. The numerical method is formulated by solving governing equations in terms of the conservations of mass and momentum considering isotropic and linear strain softening materials. Ability of this framework to simulate a complete landslide evolution, including the initiation and growth of slip surface, global slab failure, post-failure behaviours and re-deposition, has been demonstrated for different slope geometries. The proposed numerical scheme is able to capture diverse post-failure behaviours, such as retrogression and blocky slide mass, in sensitive soils. The characteristics of the slip surface growth within a favoured layer and the patterns of the global slab failure in the overlying layer have been thoroughly discussed. For planar slopes, it helps to establish an analytical criterion for unstable dynamic growth of a planar slip surface, which can optimise the slope stability analysis in sensitive soils.

Keywords: submarine landslides, landslide evolution, landslide dynamics, slip surface growth, 3D slope geometry

PLAIN LANGUAGE SUMMARY

Submarine landslides can be tens of kilometres long but may originate from a relatively small initial slip surface, growing within a 'sandwiched' weak layer. The physical mechanisms causing the slip surface growth and the whole evolution of submarine landslides are difficult to assess even with the help of state-of-the-art geophysical and geological investigations. Advanced numerical modelling is a useful tool to improve our understanding of the three-dimensional (3D) evolution of submarine landslides. Here, we propose such an original numerical method formulated from the fundamental physical laws and simulate the entire landslide evolution from slip surface growth to failure of the sliding layer and its post-failure behaviour with final re-deposition of slide mass. We optimise the assessment of the critical slip surface size for catastrophic failure, which may facilitate safe offshore and coastal development, e.g., for offshore renewables. Our criterion shows, upon certain conditions, that a slip surface can grow at considerable velocities and become as large as ~100 km^2 within minutes. This is followed by global failure and post-failure evolution, such as extended failure upslope and fan heaving downslope. The numerical replication of submarine landslide evolution improves our understanding of the complex cascading mass movement mechanisms of submarine landslides.

INTRODUCTION

Layered marine sediments usually exhibit reduction in strength during shearing, because of the collapse of the inter-particle bonding structures and the accumulation of pore water pressure. The ratio between the initial (peak) and softened (residual) strengths of marine soil sediments is usually between 3 to 7, and such soil with strength sensitive to shearing is referred to as 'sensitive soil' (Skempton 1985, L'Heureux et al. 2012, Issler et al. 2015). For slope failure in marine sensitive soils, shearing failure within a basal slip surface might lead to the growth of the slip surface, eventually evolving into a huge translational landslide such as the well-known enormous Storegga Slide (Kvalstad et al. 2005, Micallef et al. 2007) or the massive retrogressive landslide in December 2020 at Gjerdrum, Norway, which caused seven deaths.

Figure 1 shows a conceptual evolution of typical translational submarine landslides. Although their scales are usually very large, e.g. the Storegga Slide covered between 2500 and 3500 km^2 of sediment (Haflidason et al. 2004), translational slides might be initiated at a minute slip surface, as shown in Figure 1a, triggered by external factors such as earthquakes. An initial slip surface is often concentrated in a favoured soil layer (the so-called 'weak layer') where shear strength relative to the overburden pressure is lower than adjacent layers. The weak layer provides a locus for progressive growth of the slip surface with extensive external triggers, as shown in Figure 1b. Once the size of the slip surface reaches a threshold, the slip surface growth becomes catastrophic and can only be limited by slope flattening or global slab failure (see Figure 1c). Diverse post-failure behaviours, such as retrogression upslope and progressive ploughing or debris flow downslope, may present after the global slab failure (Zhang et al. 2021), as illustrated in Figure 1d.

Submarine slope stability analysis and assessment of landslide dynamics and impact to offshore infrastructure are important areas of study for engineering geology professionals and geotechnical engineers. In practice, slop stability (failure initiation) is usually simplified as a

two-dimensional (2D) plane strain problem (e.g., Morgenstern and Price 1965, Spencer 1967, Cornforth 2005), which has been considered conservative in the Limit Equilibrium Method (LEM), as resistances from the out-of-plane direction are ignored. However, the slip surface of translational landslides can grow in any direction within a favoured 'weak' layer, which may or may not be parallel to the main travel direction of the slide mass as depicted in Figure 1. Such a multi-directional propagation mechanism can provide additional driving force because of the reduction in strength during slip surface growth, but this physical failure mechanism cannot be considered in a 2D case and remains poorly understood.

Moreover, the 2D simplification needs the justification that the linear cross section chosen from a three-dimensional (3D) ground is the most 'pessimistic' (Duncan 1996). This is not an easy task in realistic complex terrain, where the most pessimistic section, if it can be found, is most likely nonlinear. To partly avoid such a geometrical uncertainty, slope stability analysis might, in practice, be conducted for multiple cross sections of a single slope, which could be a huge workload for risk assessment and mapping of a large area involved in an engineering project such as the determination of a subsea pipeline route. A practical and effective criterion considering 3D slope geometry may facilitate risk assessment of submarine landslide and help safe offshore developments.

Therefore, the main aims of the study are to discover the true physical mechanism of multi-directional slip surface growth leading to submarine landslides and to establish practical criteria for slope stability analysis in marine sensitive soils. To achieve so, the whole evolution of 3D submarine landslides, covering the failure initiation, slip surface growth, slab failure and post-failure behaviours, is observed and discussed through an original Lagrangian-Eulerian depth integrated numerical analysis. The governing equations of the problem are formulated based on conservation of mass and momentum. The solutions of landslide dynamics are obtained from a finite volume scheme with a staggered mesh strategy. New criteria for slip surface

127 growth in planar slopes are proposed and characteristics of slab failure are discussed based on
128 the numerical investigations, which are expected to facilitate slope stability analysis and risk
129 assessment of submarine landslides in sensitive soils. Finally, the ability of the framework to
130 account for the effects of the true 3D slope geometry is demonstrated.

131 **METHODS**

132 ***Existing methods for analysing submarine landslide initiation and dynamics***

133 Because of greater computational capacity, numerical studies have been able to consider 3D
134 slope stability analysis in the last several decades (Hungr et al. 1989, Lam and Fredlund 1993,
135 Huang and Tsai 2000, Cheng and Yip 2007), although most of them have focused on rotational
136 slide mechanisms using the LEMs. Some more sophisticated 3D models for slope stability
137 problems have been emerging that use numerical methods such as the Finite Element Method
138 (Griffiths and Marquez 2007, Lin et al. 2020) and Finite Difference Method (Zhang et al. 2013).

139 The LEM and most existing numerical methods reach their limits in carrying out satisfactory
140 stability analyses of submarine slopes with sensitive clays against potential translational
141 landslides, due to the progressive failure process and large deformation involved (Puzrin et al.
142 2004, 2016, Locat et al. 2011, Zhang et al. 2015). Instead, some recent studies have explored
143 simplified analytical criteria for 3D translational landslide initiation in sensitive clays by
144 interpretation and quantification of slip surface growth along a weak layer (Zhang et al. 2020,
145 Klein and Puzrin 2021), based on planar or idealised conical geometry and static conditions.
146 The applicability of these criteria to realistic slope conditions and complex geometry remains
147 uncertain.

148 Another important issue in assessing the risk of slope instability is the modelling of landslide
149 dynamics and its evolution, which can be performed by using large deformation numerical
150 methods such as the depth-integrated method (Hungr 1995, Liu and Huang 2006, Zhang and

Puzrin 2021), computational fluid dynamics (Biscarini 2010), smoothed particle hydrodynamics (Zhang et al. 2020) or the material point method (Dong et al. 2017). However, most of these are 2D in nature and need the input of details of the initial slide mass such as geometry, volume and initial velocity, which are rarely determined in practice.

A correlation between slope stability analysis (landslide initiation) and evolved debris flow (landslide dynamics) in 3D is required for fully understanding 3D landslide evolution and hence for optimised risk assessment, which will be for the first time addressed in the study.

Governing equations

In order to analyse slope stability and evolution of landslides in sensitive soils, the domain of interest is essentially divided into regularised cells, with each cell holding characteristics of the evolving landslide, as shown in Figure 2. Note that the bathymetry map, showing a submarine landslide offshore Scotland (after Carter et al. 2020) is just for illustration. The edges of the cell are parallel to the axes of coordinates x and y, and the x–y plane ($z = 0$) was set as the horizontal plane and crossing through a reference point (taken as the slope centre in the study) at the basal slip surface. Cells are fixed during the landslide process, with materials travelling through them, forming a Eulerian framework. Conservations of mass and momentum are then formulated within each cell, and global instability can be modelled by integrating all cells with consideration of proper inter-cell constitutive models and fluxes.

Key assumptions for establishing governing equations are as follows.

- The thickness of the landslide is small (<1:10) compared to its dimensions, so that the velocity can be averaged along the depth of each cell.
- Momentum of the slide mass along the z-direction is negligible.
- Trapped water moves together with soils in each cell, and any generated pore pressures have no time to dissipate, ensuring an undrained (and incompressible) condition.

175 Based on these assumptions, conservation of mass in each cell can be expressed by

$$\frac{\partial h}{\partial t}+\frac{\partial hu}{\partial x}+\frac{\partial hv}{\partial y}=0 \tag{1}$$

176 where h is the height of the cell, u and v are the velocity in the x- and y-directions (as shown
177 in Figure 2), respectively, and t is the elapsed time. Conservation of momentum in each cell is
178 given by

$$\frac{\partial hu}{\partial t}+\frac{\partial hu^2}{\partial x}+\frac{\partial h\sigma_x}{\rho\partial x}+\frac{\partial huv}{\partial y}-\frac{\partial h\tau_{xy}}{\rho\partial y}-\frac{\tau_{w,x}+\tau_{g,x}+\tau_{drag,x}}{\rho}=0 \tag{2}$$

179 and

$$\frac{\partial hv}{\partial t}+\frac{\partial hv^2}{\partial y}+\frac{\partial h\sigma_y}{\rho\partial y}+\frac{\partial huv}{\partial x}-\frac{\partial h\tau_{xy}}{\rho\partial x}-\frac{\tau_{w,y}+\tau_{g,y}+\tau_{drag,y}}{\rho}=0 \tag{3}$$

180 for the x- and y-directions, respectively. In the above equations, σ_x, σ_y and τ_{xy} are stress
181 components applied at the centre of the cell face, with the face normals parallel to the x or y
182 axis; $\tau_{\mathrm{w},x}$ and $\tau_{\mathrm{w},y}$ are weak layer (or slip surface) shear stress components; $\tau_{\mathrm{g},x}$ and $\tau_{\mathrm{g},y}$ are
183 gravity shear stress components at the buried depth of the weak layer; and $\tau_{\mathrm{drag},x}$ and $\tau_{\mathrm{drag},y}$
184 are drag shear stress components.

185 The governing equations are solved through a finite volume scheme with a staggered mesh
186 strategy, which is detailed in the Appendix. Determinations and numerical treatments of marine
187 sediment properties and drag forces from the ambient sea water are also fully addressed in the
188 Appendix, with briefs given as follows.

189 ***Marine sediment properties***

190 In addition to solving the governing equations of dynamics of the sliding layer, the changes in
191 soil properties of slip surface (within the weak layer) during the landslide process are
192 considered. The soil properties, such as stress and strength, in the weak layer are updated in the
193 fixed mesh scheme based on the current values of h, u and v, assuming that the weak layer

does not move with the sliding layer. As the sliding layer moves during the landslide process, its soil properties are updated at the deformed cell centre (based on current values of u and v) and interpolated to the original fixed centre after each time increment, in the spirit of the Arbitrary Lagrangian-Eulerian method. To this end, the numerical scheme proposed here is hereafter called the Lagrangian-Eulerian depth integrated method (LEDIM).

Within the slip surface, the shear stress (τ_{w}) is limited to the current shear strength, which is reduced during shearing, and given by

$$\tau_w = s_{uw}(\delta^p) = max\left(1 - \frac{\delta^p}{\delta_r^p}, \quad \frac{1}{S_t}\right) \cdot s_{uw,p} \tag{4}$$

where $\delta^{\mathrm{p}} = \int_0^t \left\| \dot{\boldsymbol{\delta}}^{\mathrm{p}} \right\| dt$ is the accumulated plastic shear displacement across the weak layer, $\delta_{\mathrm{r}}^{\mathrm{p}}$ the value of δ^{p} at the residual shear stress, and $s_{\mathrm{uw,p}}$ the peak undrained shear strength in the weak layer. Considering a linear and isotropic elasticity model, the pre-peak shear stress can be expressed by

$$\boldsymbol{\tau}_w = K\boldsymbol{\delta}^e \tag{5}$$

where K is the shear stiffness and δ^{e} is the elastic component of the shear displacement across the weak layer.

Hydrodynamic pressure drag for a streamlined body like a submarine sliding mass is less significant than the skin friction drag, and the latter can be approximated by (Norem et al. 1990, Elverhoi et al. 2005)

$$\tau_{drag} = \frac{1}{2} C_f \rho_w v^2; \; C_f = \left(1.89 + 1.62\, log\frac{L}{k}\right)^{-2.5} \tag{6}$$

where C_{f} is the frictional drag coefficient, ρ_{w} is the seawater density, L is the sliding mass length and k is the roughness length of the sliding mass surface in the range of 0.01–0.1 m. For a length of the sliding mass varying between 10 and 1000 m, the friction drag coefficient falls

in the range of 0.005–0.016.

Verification

A series of 2D landslides with 1D slip surface growth along a weak layer, studied in Zhang et al. (2019), were re-simulated using the proposed numerical scheme to verify its accuracy. The governing equations are tailored to fit for the 2D problems by ignoring the momentum in the *y*-direction (assuming the slide mass travels in the *x*-direction) and considering only one row of cells (assuming the problem is of plane strain nature). The numerical results from the proposed numerical scheme are compared with the observations from the large deformation finite element (LDFE) modelling by Zhang et al. (2019).

A curvilinear slope model composed of an overlying layer and a weak layer was used, as shown in Figure 3a. The weak layer is parallel to the slope surface and antisymmetric about the slope centre, which is set as the origin of the coordinate system. The weak layer geometry is described by

$$z = \begin{cases} -H\left[1 - exp\left(\frac{y}{H} tan\,\theta_c\right)\right], & y < 0 \\ H\left[1 - exp\left(-\frac{y}{H} tan\,\theta_c\right)\right], & y \geq 0 \end{cases} \tag{7}$$

where θ_{c} is the maximum slope angle at the centre, and H is the half-height of the slope.

The length of the model was set to 8,000 m so that the slope angles at two ends approach zero. The soil properties are the same as those in Zhang et al. (2019) and are listed in Table 1. For a curvilinear slope, plastic deformation is initiated at the steepest point once the maximum gravity shear stress exceeds the peak undrained shear strength. In the benchmark cases, the peak undrained shear strength of the weak layer soil is fixed at $s_{\mathrm{uw,p}} = 10$ kPa, which is small enough to achieve catastrophic slip surface growth along the weak layer, according to the criterion of Zhang et al. (2015). The undrained shear strength of the sliding layer, however, varies between $s_{\mathrm{us,p}} = 10$, 20, 30 and 100 kPa, to simulate different post-failure behaviours.

For $s_{\mathrm{us,p}} = 100$ kPa, the sliding layer is strong enough to remain stable, with the failure concentrated within the weak layer only. The evolution of the length of the slip surface is shown in Figure 3b for both LEDIM and LDFE modelling. The slip surface firstly increases and stops with a final length of 2,350 m. The results from the two numerical methods compare well overall, although the growth of the slip surface is slightly slower, and the final slip surface length is about 2% higher in the LDFE analysis. This validates the accuracy of the proposed method in simulating the slip surface growth in the weak layer.

For the other three cases with $s_{\mathrm{us,p}} = 10,\ 20$ and 30 kPa, active and passive failure are apparent at the upslope and downslope portion of the slope, respectively, as shown in Figure 4. Figure 4 also compares the upslope and downslope segments of the slip surface in the weak layer at the final stage according to the two numerical methods. With $s_{\mathrm{us,p}} = 10$ kPa, the upper layer soils are soft and flow downward after the global slab failure, with the layer becoming thinner upslope and thicker downslope. The relative strong sliding layer with $s_{\mathrm{us,p}} = 20$ and 30 kPa leads to break-up of the layer and a main scarp somewhere upslope. The proposed numerical method can generally simulate the same post-failure behaviours as the LDFE method, which further validates the method in modelling global failure.

The LDFE method is rather inefficient in simulating a 3D landslide process because of current computational capacity and the difficulty in treating a highly distorted slope surface. The proposed numerical method has a particular advantage in computational efficiency which enables it to simulate the evolution of a 3D translational landslide in sensitive soils, as will be demonstrated in the remainder of the paper.

Slope geometry

Four types of submarine slopes (planar, S-shape, convex, and concave, as shown in Figure 5) are used in the study. All of them consist of a continental shelf, a continental slope, and a

continental rise from nearshore to deep sea, with an overlying layer, a weak layer, and a base. An initial slip surface was assumed to occur within the weak layer at the centre of the continental slope. The continental slope is assumed to have an average inclination of 6° to horizontal, and the continental shelf and continental rise are horizontal. Investigations of slip surface growth and slab failure initiation focus on the planar continental slope, which is assumed sufficiently long (8,000 m) and wide (6,000 m). The complete landslide evolution, including the post-failure behaviours and the arrest of mass transport deposit, is then simulated with considerations of the full slope model and different 3D slope geometries.

A local Cartesian coordinate system *x*-*y*-*z* is used, with the origin set at the slope centre and the *z*-axis pointing away from the seabed as shown in Figure 5. The expression of the planar slope geometry is straightforward with the coordinate z linearly varying from the slope crest to the toe. To describe the S-shape slope geometry, the exponential function (7), extending through the *x*-axis, is used. The convex and concave slope geometries are constructed from a truncated cone and expressed, in terms of a global Cartesian coordinate system *X*-*Y*-*Z* as shown in Figure 5c and d, by

$$Z = 2H\left(1 - \frac{\sqrt{X^2 + Y^2} - R_t}{R_b - R_t}\right) \tag{8}$$

and

$$Z = 2H\frac{\sqrt{X^2 + Y^2} - R_b}{R_t - R_b} \tag{9}$$

where R_t and R_b are radii of circular cross sections of the truncated cone through the slope crest and the slope toe, respectively. The local coordinates can then be easily related to the global coordinates based on the origin shifting as shown in Figure 5c and d.

RESULTS

In this section, the numerical results of submarine landslide evolution are presented covering the initiation and growth of slip surface, slab failure, post-failure evolution and arrest.

Initiation of slip surface

The initial local slip surface occurs where the permanent or transient driving force exceeds the resistance. It forms either because of an increase in the driving force, e.g., by seismic events or diapirs, or a decrease in shear strength, e.g., by soil degradation or accumulation of pore pressures. In this first study, it is sufficient to assume the initial slip surface is symmetric, and its boundary can be described by a series of functions:

$$\left|\frac{2x}{l_x}\right|^n + \left|\frac{2y}{l_y}\right|^n = 1 \tag{10}$$

where n is a shape parameter, and l_x and l_y are dimensions of the slip surface in the *x*- and *y*-directions, respectively. The value of n is larger than unity for a convex slip surface. For n = 1 and 2, the boundary of the slip surface is a rhombus and an ellipse, respectively. As *n* increases, the pre-softened zone extends further and further outward, and as $n \rightarrow \infty$, the boundary becomes rectangular. For most cases studied here, the value of n was taken as 2. The shear strength in the initial slip surface might be reduced from the peak to the residual by slip weakening, time weakening or both, although the process may take a long time. Therefore, it is sufficient and conservative to assume that the shear strength in the slip surface has been reduced to the residual.

The force imbalance from the slip surface can be transferred and sustained by surrounding soils, which may undergo plastic failure and fall into the post-peak strain softening state. Figure 6 shows the contour of shear strength after the formation of a circular slip surface ($n = 2$, and $l_x = l_y = 40$ m), as simulated by using the proposed numerical scheme. At the initial state, the

300 undrained shear strength is reduced to the residual at the slip surface while being maintained
301 at the peak elsewhere. Other properties of the numerical model and materials are listed in Table
302 2. Within the weak layer, three zones can be identified as shown in the figure: the intact zone
303 (where soils remain intact), the 'process zone' (where soils undergo strain softening, and shear
304 strength ranges between the peak and the residual) and the slip surface (where soils reach the
305 residual state). Six cross sections, three in each (x- or y-) direction, are chosen to further observe
306 the distribution of the shear strength within the three zones, as given in Figure 6b and c. For
307 the x-I, x-II, y-I and y-II sections which cross all three zones, discontinuities in the distributions
308 of the shear strength exist, dropping from a post-peak value to the residual. These distinguish
309 the process zone from the initial slip surface. The x-III and y-III profiles, however, cross the
310 process zone and intact zone only, and the discontinuity in shear strength distribution is absent.
311 Note that, in this case, the process zone is developed to fully resist the unbalanced forces from
312 the slip surface, and hence the slope remains stable. This is defined as stable slip surface growth
313 and will be detailed in the next sub-section.

314 **Stable growth of slip surface**

315 Figure 7 shows under what conditions a process zone might be initiated and developed. For a
316 relatively large slip surface (i.e., $l_x = 40$ m for a circular slip surface), it can disturb and
317 weaken adjacent soils, leading to the development of a process zone surrounding the slip
318 surface. However, if the slip surface is sufficiently small (e.g., $l_x = 20$ m), the driving force
319 from the slip surface might be easily sustained by the surrounding soils without the formation
320 of the process zone, i.e., the soils remain intact as shown in Figure 7. When the diameter of the
321 slip surface grows to $l_x = 30$ m, the process zone appears only at the front and rear of the slip
322 surface.

323 The above observation reveals that: 1) for a circular slip surface, the process zone firstly
324 emerges at the rear and in front of the slip surface; and 2) the larger the slip surface, the more

significant the process zone. Figure 7 also compares the shear stress contours resulting from different sizes of slip surface. The shear stress remains the gravity value (≈6 kPa for parameters listed in Table 2) and increases to the peak at the interface between the intact and process zones. It is limited to the shear strength within the process zone and the slip surface.

Stability can be eventually achieved for the cases of $l_x = 20$, 30 and 40 m despite the development of the process zone. As defined above, the process of extensive expansion of the slip surface up to $l_x = 40$ m can be termed stable slip surface growth. In contrast, for the case of $l_x = 50$ m, the growth of the slip surface cannot be restricted under existing forces and hence is termed unstable slip surface growth. Note that Figure 7 shows a transient moment of this case, and the dynamic expansion of the slip surface during unstable slip surface growth will be discussed in the next section.

Unstable growth of slip surface

With an initial slip surface of $l_x = l_y = 50$ m and other properties listed in Table 2, the growth of the slip surface is unstable and can only be limited by slope flattening or global slab failure. Figure 8a, b and c, respectively, shows the evolution of the shear strength contour, horizontal velocity field and vertical velocity field during the unstable growth of the slip surface. To intensively investigate the slip surface growth without slab failure, the shear strength in the overlying layer was intentionally set to a high value (1,000 kPa). At $t = 10$ s, the slip surface grows from a circle to an ellipse with the major axis parallel to the potential travel direction. Thereafter, the slip surface grows dramatically and propagates more outward at the four shoulders, forming a distinctive 'peanut' shape at $t = 25$ s. The wide shoulders are generated because of larger horizontal velocity in these areas, whereas along the major (*y*-) and minor (*x*-) axes of the slip surface, the horizontal velocity is close to zero, as shown in Figure 8b. The slip surface is symmetric in terms of both *x*- and *y*-axes before $t = 50$ s. At $t = 50$ s, however, the downslope part of the slip surface is slightly larger than the upslope, as soil begins to be

accumulated more downslope.

Slab failure

Figure 9 shows the slab failure with respect to the contours of the plastic strain and deviatoric stress in the overlying layer, together with the slip surface growth with respect to the contours of the shear strength in the weak layer. Note that the at-rest lateral earth pressure coefficient, which is the horizontal earth pressure over the vertical earth pressure, was set to $K_0 = 0.5$. The peak undrained shear strength was fixed at $s_{\mathrm{uw,p}} = s_{\mathrm{us,p}} = 10$ kPa for this case. At $t = 5$ s, slab failure emerges at the rear of the slip surface where soils are unloaded and the deviatoric stress reaches the maximum 20 kPa; while in front of the slip surface, soils are loaded and the deviatoric stress decreases from the initial value. At $t = 10$ s, the soils in front of the slip surface have been loaded to the (passive) failure state, and, accordingly, the deviatoric stress also reaches the maximum. Thereafter, the slab failure propagates mainly at the downslope portion with diffusive plastic strain; at the rear of the slip surface, the plastic strains are accumulated, but the propagation of the slab failure is not apparent. Rather than like a fan zone formed in front of the slip surface, the rear boundary of the slip surface (or the main scarp) is quite straight. For the planar slope studied here, the slip surface keeps growing along the *x*-direction, with the side boundaries of the slip surface continuing to extend further outward.

Post-failure evolution and arrest of landslide

It has been demonstrated above that, once initiated, the slip surface growth and slab failure propagation cannot be arrested on a planar continental slope. Either slope flattening or material strengthening can restrict slip surface growth and slab failure propagation. To further observe the arrest of slip surface and post-failure behaviours, the full slope model including a relatively flat continental shelf and a continental rise, as shown in Figure 5, is used. It consists of a continental slope with a slope angle of 6° and length of 400 m (coordinate y from −200 m to 200 m), a flat continental shelf (y <−200 m) and a flat continental rise ($y >$ 200 m). The peak

375 undrained shear strength of the weak layer soil, the weak layer depth and the submerged soil
376 unit weight were chosen as $s_{\mathrm{uw,p}} = 15$ kPa, $h = 8$ m, and $\gamma' = 8$ kN/m^3, respectively. This
377 parameter set generates a strength ratio of $s_{\mathrm{uw,p}}/\gamma' h = 0.234$, which is typical for normally
378 consolidated marine sediments. The overlying layer was assumed slightly over-consolidated
379 with a peak strength of $s_{\mathrm{us,p}} = 10$ kPa and strength ratio of 0.31. The soil sensitivities of the
380 weak layer and the overlying layer were set to 7 and 2, respectively. An elliptical initial slip
381 surface of $l_x = 40$ m and $l_y = 80$ m was pre-set. Other parameters are the same as those listed
382 in Table 2.

383 Figure 10a shows the landslide dynamic evolution from the slab failure initiation, post-failure
384 stage to re-deposition with respect to the contours of the shear strength in the weak layer and
385 the plastic strain in the overlying layer, and the changes in the overlying layer thickness. Note
386 that the normalised sliding layer thickness is calculated as the ratio of the current thickness and
387 the initial thickness of the overlying layer. At $t = 10$ s, slab failure is initiated with a certain
388 amount of slip surface growth. The plastic strain is more concentrated at the rear of the slip
389 surface, and a curved back scarp is formed at this stage, with the height of the scarp exceeding
390 4 m ($0.5h$). The main scarp moves backward with the retrogressive failure at the rear of the slip
391 surface. The retrogression is stopped by the flat continental shelf, leaving a fairly straight main
392 scarp of 200 m in length and over 4 m in height. Because of the strain softening, the failed
393 overlying mass is torn apart into blocks, within which the plastic strain of the sliding layer is
394 insignificant as shown in the second row of Figure 10a. The blocks are broken into smaller
395 pieces and finally disappear during their downward movement. The failed and softened slide
396 mass is finally deposited at the continental rise, forming a compressed fan zone of around 400
397 m in diameter and over 4 m in heave. The extent of the slip surface in the weak layer is almost
398 identical to the combined area of the source region and deposition fan zone. Features such as
399 the main scarp, the blocks seen during progressive failure, and the deposition fan zone are

consistent with site investigations of many historical submarine landslides, e.g., the Loch Eriboll Slide discovered offshore Scotland (Carter et al. 2020) and shown in Figure 10b.

DISCUSSIONS

Mechanism and evolution of translational submarine landslides

Observed from the numerical modelling, the evolution of translational submarine landslides in sensitive marine sediments can be summarised as follows.

I. *Slip surface initiation*. A slip surface might be formed and grow stably within a weak layer due to extensive external triggers such as earthquakes and excess pore pressure accumulation. Strain softening of sensitive soils during shearing leads to formation of a process zone, where undrained shear strength reduces from the peak towards the residual, surrounding the slip surface.

II. *Slip surface growth*. Once the slip surface reaches a certain size because of intensive triggers, its growth becomes unstable and catastrophic, restricted only by slope flattening or slab failure. The critical area of the slip surface for unstable growth is almost independent of its shape but depends on the material properties and shear stress ratio over the slip surface. Regardless of the initial shape, the slip surface transitions from an ellipse to a 'peanut' pattern during the unstable growth stage.

III. *Slab failure*. With the growth of the slip surface, the driving force increases, and so does the deviatoric stress within the overlying layer. Therefore, at a certain stage of the unstable slip surface growth, the overlying soils may reach the maximum allowable stress, initiating slab failure. After the slab failure, the growth of the slip surface is in alignment with the propagation of the slab failure.

IV. *Post-failure evolution*. A main scarp forms at the rear of the slip surface after the slab failure, and is followed by retrogression, which is limited by upslope slope flattening.

The failed slide mass disintegrates into blocks and then turns to fully softened debris flow with downward movement. The slide mass finally re-deposits at the flat terrain with the mass transport deposit forming a fan zone.

Features of dynamic slip surface evolution

Slip surface growth pattern

The pattern of stable growth of the slip surface depends on the shape of the initial slip surface. Figure 11 shows the different patterns of stable slip surface growth for elliptical slip surfaces with different ratios of major and minor axes, in terms of the shear strength contour. Similar to Figure 6b and c, Figure 12 presents the distributions of shear strength along the major and minor axes of the slip surface to visualise the growth pattern of the slip surface. In all cases, the stable growth of the slip surface together with the development of the process zone is obvious. As demonstrated above, for a circular slip surface with $l_x/l_y = 1$, the travel direction (x-direction) is the favoured direction for slip surface growth. The favoured direction along the x-direction of growth is enhanced with a larger axis ratio (a wider slip surface), e.g., $l_x/l_y = 2$. For a slender slip surface (of small axis ratio, $l_x/l_y = 0.25$), however, the slip surface tends to propagate along the y-direction first, presenting a different growth pattern from wide slip surfaces. For instance, with $l_x = 20$ m and $l_y = 60$ m, soil at the two sides of the slip surface begins to soften while the soil in front and at the rear of the slip surface remains intact. With the axis ratio $l_x/l_y = 0.5$, the slip surface seems to grow simultaneously along the periphery of the slip surface without an obvious favoured direction, which forms the most pessimistic situation.

Figure 13 briefly illustrates the three modes. The growth of the slip surface along the *x*-direction is driven by the compression force downslope and extension force upslope, akin to the in-plane shear mode of crack propagation in fracture mechanics (i.e., a shear stress acting parallel to the

plane of the slip surface and perpendicular to the slip surface front); while the growth along the *y*-direction is driven by the shear force, akin to the out-of-plane shear mode of crack propagation in the fracture mechanics (i.e., a shear stress acting parallel to the plane of the slip surface and parallel to the slip surface front). Here, the former is defined as the compression-extension mode and the latter is defined as the shear mode. In reality, a combined mode including both the compression-extension and shear modes is expected to be more common, particularly when the slip surface growth is unstable and continuous. It has not been possible to study the shear and combined modes in previous 2D investigations (e.g., Puzrin et al. 2004, Kvalstad et al. 2005, Zhang et al. 2015).

Zhang et al. (2020) assumed that the (horizontal) velocity of the slide mass along the *x*-direction is negligible compared to the *y*-direction component, which has been found to be a robust result during the stable growth of slip surface through LDFE modelling. This generates a plane strain condition with the compression/extension modulus in the sliding layer calculated by

$$E_{ps} = \frac{E}{1-\nu^2} = \frac{2G}{1-\nu} \tag{11}$$

where E is the Young's modulus and ν the Poisson's ratio. This assumption needs to be verified for the stage of unstable slip surface growth. To achieve this, conservation of momentum in the *x*-direction, i.e. governing equation (2), was ignored and the horizontal component of the velocity was set to zero. Numerical results of such an idealised case in terms of the strength contours are presented in Figure 8d. For $t = 5$ s and 10 s, the slip surfaces of the idealised case are almost identical to the case formulated by rigorous governing equations as shown in Figure 8a. However, with further unstable growth of the slip surface, the shape of the slip surface remains an ellipse, which is different from the 'peanut' shape of the rigorous case.

Figure 14 compares the two mechanisms at $t = 50$ s. The major and minor axes of the 'peanut'

slip surface are the same as those of the 'ellipse' slip surface, with the area of the slip surface larger in the former mechanism. The different mechanisms found in the two cases imply that the horizontal movement of the slide mass plays an important role and has to be considered during the unstable growth of the slip surface.

Slip surface growth speed

Once a slip surface falls into the unstable growth stage, the growth speed depends on how the unbalanced forces are transferred within the overlying layer. For the compression-extension mode, the growth of the slip surface is driven by the compressional/tensile force, and therefore the growth speed (of the major axis) can be related to the compression wave velocity

$$v_{maj} = 2\sqrt{\frac{E'}{\rho}} \tag{12}$$

where E' is the compression modulus. Note that the number 2 in the expression means that the growth speed is double the wave velocity, as the slip surface grows in both the upslope and downslope directions. Similarly, for the shear mode, the growth speed of the minor axis can be related to the shear wave velocity

$$v_{min} = 2\sqrt{\frac{G}{\rho}} \tag{13}$$

For plane strain and undrained conditions, the compression modulus, $E' = E_{\mathrm{ps}}$, is four times the shear modulus (see equation (11)) and therefore, the major axis always doubles the minor axis of the slip surface. This can be seen in Figure 14, where the major axes of the slip surfaces are almost 3,000 m while the minor axes are around 1,500 m in both mechanisms.

Figure 15a shows the length (major axis) and width (minor axis) of the slip surface during its growth for the selected case, compared with the analytical solutions given by equations (12) and (13). It should be noted that the growth of the slip surface evolves from the stable to

unstable stages with the transition emerging at around $t = 4$ s. During the stable growth stage, both axes of the slip surface are assumed unchanged. With this idealisation, the growth of the two axes of the slip surface in the numerical modelling can be well predicted by the analytical solutions, with the growth speeds being 34 m/s and 68 m/s for the minor and major axes, respectively. Such fast speeds reveal that unstable growth of the slip surface is catastrophic and significantly differs from creep failure.

Figure 15b gives the area of the slip surface during its unstable growth for both mechanisms. For the 'ellipse' mechanism, the area can be calculated exactly by

$$A = \frac{\pi}{4} l_x l_y \tag{14}$$

which is shown by the good agreement between the numerical and analytical results in the figure. The area of the ellipse slip surface is initially 1,962.5 m^2 and increases to 3.6 km^2 in 50 s. The peanut slip surface (5.3 km^2) is about 45% larger than the ellipse slip surface at $t = 50$ s. The fast growth of the slip surface implies that during an earthquake, even with a short period of shaking, a large slip surface with a magnitude of ~ km^2 might be formed. Such a large slip surface may further result in global slab failure and debris flow. Therefore, it is key to determine in what conditions the slip surface can grow unstably, which will be discussed in the next sub-section.

Criteria for unstable growth of slip surface

For a slip surface described by a series of functions (10), the area of the slip surface can be calculated by

$$A = \frac{l_x l_y}{n} \cdot \frac{\Gamma(1 + 1/n)\Gamma(1/n)}{\Gamma(1 + 2/n)} \tag{15}$$

where Γ is the gamma function. By integrating the normal and shear resistances along the boundary of the slip surface, one may calculate the total resistance and compare it to the driving

512 force from the slip surface, whereby the critical area of the slip surface for unstable growth is
513 given by (Zhang et al. 2020)

$$A_{cri} = 32\left(\frac{1-r}{r}l_c\right)^2 \tag{16}$$

514 where r is the shear stress ratio and l_c is the critical length relevant to the process zone size,
515 given by

$$r = \frac{\tau_g - s_{uw,r}}{s_{uw,p} - s_{uw,r}}, l_c = \sqrt{\frac{Gh\delta_r^p}{s_{uw,p} - s_{uw,r}}} \tag{17}$$

516 For static analysis, ignoring any inertia effects, the criterion (16) is conservative compared to
517 the numerical data from finite element and finite difference modelling (Zhang et al. 2020).

518 A parametric study was conducted to observe the effects of the shape parameter, n, and the
519 dimensions of the slip surface on the critical area for unstable slip surface growth. The gravity
520 loads and the critical surface areas at critical conditions for all cases are presented in Table 3.
521 Figure 16a shows a comparison of the numerical results with or without inertia effects and the
522 analytical results by criterion (16). In dynamic analysis conducted in the current study, the
523 critical area estimated by (16) is not always conservative, particularly with a large shear stress
524 ratio. Assuming that the dynamic criterion meets the same series of functions as the static
525 criterion (16), the best fit of the numerical data from the dynamic analysis gives

$$A_{cri} = 18.4\left(\frac{1-r}{r}l_c\right)^2 \tag{18}$$

526 which is shown in Figure 16b. This means that the critical area of the slip surface for unstable
527 slip surface growth under dynamic conditions is on average 42.5% smaller than that ignoring
528 inertia effects. This echoes the finding that in a 2D plane strain slope, the critical length (major
529 axis) of slip surface for catastrophic propagation can be up to 50% lower with inertia effects
530 than without inertia effects (Zhang et al. 2016). Extending this observation to the 3D case, one

may simply assume for the dynamic unstable growth a 50% reduction in the critical area of the slip surface from the static criterion (18), that is

$$A_{cri} = 16\left(\frac{1-r}{r} l_c\right)^2 \tag{19}$$

Figure 16a shows that the criterion (19) gives estimates of the critical slip surface area well below the numerical data and is therefore conservative.

Slip surface growth *vs* slab failure

Growth of the slip surface within the weak layer and slab failure within the overlying layer are two competing mechanisms leading to large-scale landslides in sensitive soils. The extent of the slip surface depends on how 'weak' the weak layer is. With the growth of the slip surface, the driving force increases, and so does the deviatoric stress within the overlying layer given by equations (26) and (27). Therefore, at a certain stage of the unstable slip surface growth, the overlying soils may reach the maximum allowable deviatoric stress, initiating slab failure.

Figure 17 shows the increase of the maximum deviatoric stress of the overlying soils with the growth of the slip surface. The peak undrained shear strength of the weak layer soil was fixed at $s_{\mathrm{uw,p}} = 10$ kPa, while the strength of the overlying soil, $s_{\mathrm{us,p}}$, was varied between 10 kPa, 20 kPa, 50 kPa, 100 kPa and 1,000 kPa without strain softening. The other parameters remain the same as those in Table 2. At the initial state, the deviatoric stress is 26 kPa, which is essential to make the slip surface grow unstably from an initial area of 2,352 m^2 (with $l_x = 40$ m and $l_y = 80$ m). In the case of $s_{\mathrm{us,p}}/s_{\mathrm{uw,p}} = 100$, the 'unrealistic' strong overlying layer leads to the pure growth of the slip surface over the whole simulation domain (8,000 m × 6,000 m), and the deviatoric stress keeps growing, as shown in the figure. For the other cases, the deviatoric stress is limited to $2s_{\mathrm{us,p}}$, which satisfies the generalised nature of the von Mises failure criterion with respect to the Tresca failure criterion. The stronger the overlying soil, the larger the slip surface at the initiation of slab failure. For example, the slip surface at the slab

554 failure initiation is as large as 1.1 km^2 in the case of $s_{\mathrm{us,p}}/s_{\mathrm{uw,p}} = 10$, while it is reduced by
555 2/3 when the undrained shear strength of the overlying soil is decreased by half. When the
556 weak layer is not literally 'weak', i.e., in the case of $s_{\mathrm{us,p}}/s_{\mathrm{uw,p}} = 1$, the slab failure is triggered
557 without unstable growth of the slip surface, as the required deviatoric stress (26 kPa) is
558 essentially higher than the maximum allowable value ($2s_{\mathrm{us,p}} = 20$ kPa).

559 Figure 18 compares the slip surface and slab failure at $t = 50$ s for cases with different strength
560 ratios, $s_{\mathrm{us,p}}/s_{\mathrm{uw,p}} = 1, 2, 5, 10$. For the case of the strongest overlying layer ($s_{\mathrm{us,p}}/s_{\mathrm{uw,p}} =$
561 10), the slab failure initiates only at the rear and the sides of the growing slip surface. With the
562 decrease of the overlying soil strength, the downslope portion fails together with the upslope
563 portion. The slip surface pattern of the downslope portion does not alter significantly, although
564 the accumulated plastic strain in the overlying layer decreases with the increase of the overlying
565 soil strength. A 'peanut' slip surface mechanism remains for $s_{\mathrm{us,p}}/s_{\mathrm{uw,p}} = 2, 5, 10$ before the
566 slab failure; while for $s_{\mathrm{us,p}}/s_{\mathrm{uw,p}} = 1$, only the bottom half of the 'peanut' is developed as the
567 slab failure occurs early and stops the growth of the slip surface upslope. The upper half of the
568 slip surface, however, becomes flat and propagates less after the slab failure.

569 ***Effects of a 3D slope geometry***

570 Three typical 3D slope types, as shown in Figure 5b, c and d, are considered in this section in
571 order to gain an initial insight into the slope geometry effects on the translational landslide
572 evolution. For the S-shape slope, the half-height of the slope in equation (7) was set to be the
573 same as for the planar slope, i.e., $H = 21$ m, and the maximum slope angle was taken as $\theta_c =$
574 9° such that the average slope angle within the range of -500 m $< y <$ 500 m is equal to the
575 planar slope angle of 6°. For the convex slope, the values of R_t and R_b were set to 800 m and
576 1,200 m, respectively; while for the concave slope, $R_b = 800$ m and $R_t = 1{,}200$ m. The slope
577 angle of the convex and concave slope models is the same with the planar slope model.

Figure 19 compares the final states of the four slope models with respect to the fields of the shear strength in the weak layer, the shear stress in the weak layer, the plastic strain in the sliding layer, and the normalised sliding layer thickness. It can be noted that the far field gravity shear stress fields (second row of Figure 19) strongly depend on the geometry of the problem. The results of the planar, convex and concave slopes look very similar, with slightly more horizontal slip surface growth observed in the convex slope and slightly more retrogressive extension pertained in the concave slope, suggesting that the slope gradient along the x-direction has limited influence on the landslide evolution. In contrast, the final slip surface and mass transport deposit observed in the S-shape curvilinear slope are significantly different from the other three models with less extended retrogressive failure and a smaller fan heave zone. This confirms the conclusions from the previous studies (e.g., Puzrin et al. 2017, Zhang et al. 2021) that the slope gradient along the *y*-direction has a considerable effect on the landslide evolution.

The examples shown here present an initial investigation of 3D post-failure behaviours of submarine landslides in sensitive clays. Detailed investigation of the effects of the 3D slope geometry on post-failure patterns is beyond the scope of the present work and will be explored in future studies by using the proposed numerical tool.

CONCLUSIONS

This study has simulated and discussed the whole evolution of a translational landslide in a 3D slope of sensitive soils by using an original large deformation numerical tool, in order to understand the true failure mechanism and physical evolution of translational submarine landslides and establish original criteria for analysing landslide initiation. The numerical scheme has been established by solving governing equations in terms of the conservations of the mass and the momentum of sliding mass in discretised Eulerian cells of a simulation domain

602 with a depth integrated finite volume method.

603 The complete evolution of submarine translational landslides in sensitive soils includes the slip
604 surface initiation and growth along a weak layer, slab failure, post-failure behaviours and re-
605 stabilisation. A slip surface might be formed and grow stably within a weak layer due to
606 extensive external triggers such as earthquakes and excess pore pressure accumulation. The
607 growth pattern depends on the shape of initial slip surface. For an initially wide slip surface,
608 the process zone first emerges in front and at the rear of the slip surface, whereas for an initially
609 slender slip surface, it occurs at the two sides. For an elliptical slip surface, the process zone
610 develops around the periphery of the slip surface without any favoured direction. The critical
611 area of the slip surface for unstable growth is almost independent of its shape but depends on
612 the material properties and shear stress ratio over the slip surface. For planar continental slopes,
613 it is given by $A_{\mathrm{cri}} = 16\left(\frac{1-r}{r} l_{\mathrm{c}}\right)^2$ where the shear stress ratio, r, and characteristic length, l_{c},
614 are expressed by equation (17).

615 Regardless of the initial shape, the slip surface transitions from an ellipse to a 'peanut' pattern
616 during the unstable growth stage, with expansion rates equal to compression wave velocity and
617 shear wave velocity along the major and minor axes of the slip surface, respectively. The global
618 slab failure usually initiates at the rear of the slip surface if the at-rest earth pressure coefficient
619 is smaller than unity. The stronger the overlying layer, the larger the slip surface before the
620 global slab failure. A main scarp forms at the rear of the slip surface after the slab failure, and
621 is followed by retrogression, which is limited by upslope slope flattening. The slide mass finally
622 re-deposits at the flat terrain with the mass transport deposit forming a fan zone. The differences
623 in the landslide failure extension and mass transport deposit morphology between the planar,
624 the convex, and the concave slopes of the same and uniform slope angle and parallel layering
625 characteristic of sediments were found to be insignificant. In contrast, in the curvilinear slope,

626 a significantly less extended failure upslope and a smaller fan heave zone downslope have been
627 observed.

628 **ACKNOWLEDGEMENTS**

629 The authors would like to thank Prof. Mark Randolph of the University of Western Australia and
630 Prof. Dong Wang of the Ocean University of China for valuable discussions on the topic. Data used
631 in this study is publicly available at the Figshare repository 10.6084/m9.figshare.17029700.

632 **REFERENCES**

633 Biscarini, C. (2010). Computational fluid dynamics modelling of landslide generated water
634 waves. Landslides, 7: 117–124.

635 Carter, G. D. O., Cooper, R., Gafeira, J., Howe, J. A. and Long, D. (2020). Morphology of
636 small-scale submarine mass movement events across the northwest United Kingdom.
637 Geomorphology, 365: 107282.

638 Cheng, Y. M. and Yip, C. J. (2007). Three-dimensional asymmetrical slope stability analysis
639 extension of Bishop's, Janbu's, and Morgenstern–Price's Techniques. Journal of
640 Geotechnical and Geoenvironmental Engineering, 133(12): 1544–1555.

641 Cornforth, D. H. (2005). Landslides in practice: investigation, analysis and
642 remedial/preventative options in soils. John Wiley and Sons Inc., New Jersey, NJ, USA.

643 Dong, Y., Wang, D. and Randolph, M. F. (2017). Runout of submarine landslide simulated
644 with material point method. Procedia Engineering, 175: 357–364.

645 Duncan, J. M. (1996). State of the art: limit equilibrium and finite-element analysis of slopes,
646 Journal of Geotechnical Engineering, 122(7): 557–596.

647 Elverhoi, A., Issler, D., De Blasio, F.V., Ilstad., Harbitz, C.B. and T. Gauer, P. (2005).
648 Emerging insights into the dynamics of submarine debris flows. Natural Hazards and Earth
649 System Sciences, 5: 633–648.

650 Griffiths, D. V. and Marquez, R. M. (2007). Three-dimensional slope stability analysis by
651 elasto-plastic finite elements. Géotechnique, 57(6): 537–546.

Haflidason, H., Sejrup, H. P., Nygard, A., Mienert, J., Bryn, P., Lien, R., Forsberg, C. F., Berg, K. and Masson, D. (2004). The Storegga Slide: architecture, geometry and slide development. Marine Geology, 213(1–4): 201–234.

Huang, C. C. and Tsai, C. C. (2000). New method for 3D and asymmetrical slope stability analysis. Journal of Geotechnical and Geoenvironmental Engineering, 126(10): 917–927.

Hungr, O. (1995). A model for the runout analysis of rapid slides, debris flows, and avalanches. Canadian Geotechnical Journal, 32: 610–623.

Hungr, O., Salgado, F. and Byrne, P. (1989). Evaluation of a three-dimensional method of slope stability analysis. Canadian Geotechnical Journal, 26(4): 679–686.

Issler, D., L'Heureux, J.S., Cepeda, J.M. and Quan Luna, B. (2015). Towards a numerical run-out model for quick-clay slides. EGU General Assembly 2015, held 12-17 April, 2015 in Vienna, Austria.

Klein, B. and Puzrin, A. M. (2021). Growth of slip surfaces in 3D conical slopes. International Journal for Numerical and Analytical Methods in Geomechanics, Online, https://doi.org/10.1002/nag.3220.

Kvalstad, T. J., Andresen, L., Forsberg, C. F., Berg, K., Bryn, P., Wangen, M. (2005). The Storegga slide: evaluation of triggering sources and slide mechanics. Marine and Petroleum Geology, 22(1-2): 245–256.

Lam, L. and Fredlund, D. G. (1993). A general limit equilibrium model for three-dimensional slope stability analysis. Canadian Geotechnical Journal 30(6): 905–919.

L'Heureux, J.S., Longva, O., Steiner, A., Hansen, L., Vardy, M.E., Vanneste, M., Haflidason, H., Brendryen, J., Kvalstad, T.J., Forsberg, C.F., Chand, S. and Kopf, A. (2012). Identification of weak layers and their role for stability of slopes at Finneidfjord, Northern Norway. In: Yamada Y. et al. (eds) Submarine Mass Movements and Their Consequences. Advances in Natural and Technological Hazards Research, vol 31. Springer, Dordrecht.

Lin, H. D., Wang, W. C. and Li, A. J. (2020). Investigation of dilatancy angle effects on slope stability using the 3D finite element method strength reduction technique. Computers and Geotechnics, 118: 103295.

Liu, K. F. and Huang, M. C. (2006). Numerical simulation of debris flow with application on hazard area mapping. Computational Geosciences, 10(2): 221–240.

682 Locat, A., Leroueil, S., Bernander, S., Demers, D., Jostad, H.P, Ouehb, L. (2011). Progressive
683 failure in eastern Canadian and Scandinavian sensitive clays. Canadian Geotechnical
684 Journal, 48(11): 1696–1712.

685 Micallef, A., Masson, D.G., Berndt, C. and Stow, D.A.V. (2007). Morphology and mechanics
686 of submarine spreading: A case study from the Storegga Slide. Journal of Geophysical
687 Research: Earth Surface, 112: F03023.

688 Morgenstern, N. and Price, V. (1965). The analysis of the stability of general slip surfaces,
689 Géotechnique, 15(1): 79–93.

690 Norem H, Locat J, Schieldrop B (1990) An approach to the physics and the modelling of
691 submarine flowslides. Marine Georesources & Geotechnology, 9(2): 93–111.

692 Puzrin, A.M., Germanovich, L.N. and Friedli, B. (2016). Shear band propagation analysis of
693 submarine slope stability. Géotechnique, 66(3): 188–201.

694 Puzrin AM, Germanovich LN, Kim S (2004) Catastrophic failure of submerged slopes in
695 normally consolidated sediments. Géotechnique 54(10): 631–643.

696 Skempton, A.W. (1985). Residual strength of clays in landslides, folded strata and the
697 laboratory. Geotechnique, 35(1): 3–18.

698 Spencer, E. (1967). A method of analysis of stability of embankments assuming parallel inter-
699 slice forces. Géotechnique, 17(1): 11–26.

700 Zhang, W., Klein, B., Randolph, M. F. and Puzrin, A. M. (2021). Upslope failure mechanisms
701 and criteria in submarine landslides: shear band propagation, slab failure and retrogression.
702 Journal of Geophysical Research: Solid Earth, Online, DOI: 10.1029/2021JB022041

703 Zhang, W. and Puzrin, A. M. (2021). Depth integrated modelling of submarine landslide
704 evolution. Landslides, 18: 3063–3084.

705 Zhang, W., Randolph, M. F., Puzrin, A. M. and Wang, D. (2020). Criteria for planar shear band
706 propagation in submarine landslide along weak layers. Landslides, 17(4): 855–876.

707 Zhang, W., Wang, D., Randolph, M. F. and Puzrin, A. M. (2015). Catastrophic failure in planar
708 landslides with a fully softened weak zone. Géotechnique, 65(9): 755–769.

709 Zhang, W., Wang, D., Randolph, M. F. and Puzrin, A. M. (2016). Dynamic propagation criteria
710 for catastrophic failure in planar landslides. International Journal for Numerical and
711 Analytical Methods in Geomechanics, 2016, 40: 2312–2338.

712 Zhang, W., Randolph, M. F., Puzrin, A. M. and Wang, D. (2019). Transition from shear band
713 propagation to global slab failure in submarine landslides. Canadian Geotechnical Journal,
714 56(4): 554–569.

715 Zhang, Y., Chen, G., Zheng, L., Li, Y. and Zhuang, X. (2013). Effects of geometries on three
716 dimensional slope stability. Canadian Geotechnical Journal, 50(3): 233–249.

717

APPENDIX – NUMERICAL SCHEME FOR 3D MODELLING OF SUBMARINE LANDSLIDE EVOLUTION

Governing equations

Based on assumptions given in the subsection of 'governing equations', conservation of mass in each cell can be expressed by

$$\frac{\partial h}{\partial t}+\frac{\partial hu}{\partial x}+\frac{\partial hv}{\partial y}=0 \tag{20}$$

where h is the height of the cell, u and v are the velocity in the x- and y-directions (as shown in Figure 2), respectively, and t is the elapsed time. Conservation of momentum in each cell is given by

$$\frac{\partial hu}{\partial t}+\frac{\partial hu^2}{\partial x}+\frac{\partial h\sigma_x}{\rho\partial x}+\frac{\partial huv}{\partial y}-\frac{\partial h\tau_{xy}}{\rho\partial y}-\frac{\tau_{w,x}+\tau_{g,x}+\tau_{drag,x}}{\rho}=0 \tag{21}$$

and

$$\frac{\partial hv}{\partial t}+\frac{\partial hv^2}{\partial y}+\frac{\partial h\sigma_y}{\rho\partial y}+\frac{\partial huv}{\partial x}-\frac{\partial h\tau_{xy}}{\rho\partial x}-\frac{\tau_{w,y}+\tau_{g,y}+\tau_{drag,y}}{\rho}=0 \tag{22}$$

for the x- and y-directions, respectively. In the above equations, σ_x, σ_y and τ_{xy} are stress components applied at the centre of the cell face, with the face normals parallel to the x or y axis; $\tau_{\mathrm{w},x}$ and $\tau_{\mathrm{w},y}$ are weak layer (or slip surface) shear stress components; $\tau_{\mathrm{g},x}$ and $\tau_{\mathrm{g},y}$ are gravity shear stress components at the buried depth of the weak layer; and $\tau_{\mathrm{drag},x}$ and $\tau_{\mathrm{drag},y}$ are drag shear stress components.

Stress components at cell face centre

Usually, the stress tensor ($\boldsymbol{\sigma}$) describing the stress status at the centre of the cell face can be decomposed into

$$\boldsymbol{\sigma} = \boldsymbol{s} + p \cdot \boldsymbol{I} \tag{23}$$

where $\boldsymbol{s}$ is the deviatoric stress tensor, p the mean stress and $\boldsymbol{I}$ the second-order identity tensor. Note that the vertical normal stress component σ_z can be expressed by

$$\sigma_z = \frac{1}{2}\gamma' h \tag{24}$$

where γ' is the submerged unit weight of soils.

Similarly, the strain tensor ($\boldsymbol{\varepsilon}$) can be decomposed into

$$\boldsymbol{\varepsilon} = \boldsymbol{e} + \frac{\varepsilon_v}{3} \cdot \boldsymbol{I} \tag{25}$$

where $\boldsymbol{e}$ is the deviatoric strain tensor and ε_{v} the volumetric strain. It can also be divided into the elastic and plastic portions, which will be denoted by superscripts 'e' and 'p', respectively, in the remainder of the paper. Note that the volumetric strain satisfies $\varepsilon_{\mathrm{v}} = \varepsilon_{\mathrm{v}}^{\mathrm{e}} = \varepsilon_{\mathrm{v}}^{\mathrm{p}} \to 0$, as the undrained condition was maintained and the von Mises yield criterion with an associated flow rule was used. Hence, one may write $\boldsymbol{\varepsilon} \cong \boldsymbol{e}$, $\boldsymbol{\varepsilon}^{\mathrm{e}} \cong \boldsymbol{e}^{\mathrm{e}}$, and $\boldsymbol{\varepsilon}^{\mathrm{p}} \cong \boldsymbol{e}^{\mathrm{p}}$. The elasticity of materials is assumed linear and isotropic, and therefore the deviatoric stress tensor is expressed by

$$\boldsymbol{s} = 2G\boldsymbol{e}^{e} \cong 2G\boldsymbol{\varepsilon}^{e} \tag{26}$$

where G is the shear modulus.

A modified von Mises yield criterion was adopted in order to consider isotropic and linear strain softening, given by

$$q = max\left(1 - \frac{\varepsilon_s^p}{\varepsilon_{s,r}^p}, \quad \frac{1}{S_t}\right) \cdot 2s_{us,p} \tag{27}$$

where $q = \sqrt{\frac{3}{2}}\|\boldsymbol{s}\|$ is the deviatoric stress, $s_{\mathrm{us,p}}$ the peak undrained shear strength in the sliding layer which can be measured from a triaxial element test; $\varepsilon_{\mathrm{s}}^{\mathrm{p}} = \int_0^t \sqrt{\frac{2}{3}}\|\dot{\boldsymbol{e}}^{\mathrm{p}}\| dt$ the accumulated

plastic deviatoric strain; $\varepsilon_{\mathrm{s,r}}^{\mathrm{p}}$ the accumulated deviatoric strain to the residual shear strength; S_{t} the soil sensitivity defining the ratio of the peak and residual shear strengths. $\varepsilon_{\mathrm{s,r}}^{\mathrm{p}}$ can be determined from a triaxial test by $\varepsilon_{\mathrm{s,r}}^{\mathrm{p}} = \frac{2}{3}\gamma_{\mathrm{r}}^{\mathrm{p}}$ where $\gamma_{\mathrm{r}}^{\mathrm{p}}$ is the plastic shear strain associated to the residual undrained shear strength.

The softening and associated flow rules used for calculating stress components on the cell faces are also depicted in Figure A1a. The solid circle represents the current yield surface in the meridian plane while the dashed circle represents the softening yield surface. With an incremental deviatoric strain tensor, soils may move from the initial elastic state *A* to the plastic state *B* (see Figure A1a). An intermediate virtual state *T* outside the yield surfaces was assumed, in order to calculate the plastic strain. According to equations (26) and (27), one may write

$$\boldsymbol{OA} = 2G\boldsymbol{e}^{e,A};\ \boldsymbol{OB} = 2G\boldsymbol{e}^{e,B};\ \boldsymbol{AT} = 2G\Delta\boldsymbol{e};\ \boldsymbol{BT} = 2G\Delta\boldsymbol{e}^{p};\ \boldsymbol{BT}' = \frac{4}{3}\frac{s_{us,p}}{\varepsilon_{s,r}^{p}}\Delta\boldsymbol{e}^{p} \tag{28}$$

where T' is the intersect of the line BT and the current yield surface. As the radius of the current yield surface (the solid circle) is $R_{\mathrm{ys}} = \sqrt{\frac{2}{3}}d\left(\varepsilon_{\mathrm{s}}^{\mathrm{p}}\right)$, the incremental plastic deviatoric strain can then be calculated based on the geometric relationship, by

$$\begin{aligned} R_{ys} - \|\boldsymbol{BT}'\| = \|\boldsymbol{OT}\| - \|\boldsymbol{BT}\| &\rightarrow \sqrt{\frac{2}{3}}d\left(\varepsilon_{s}^{p}\right) - \frac{4}{3}\frac{s_{us,p}}{\varepsilon_{s,r}^{p}}\|\Delta\boldsymbol{e}^{p}\| \\ &= 2G\|\boldsymbol{e}^{e,A} + \Delta\boldsymbol{e}\| - 2G\|\Delta\boldsymbol{e}^{p}\| \\ &\rightarrow \|\Delta\boldsymbol{e}^{p}\| = \frac{2G\|\boldsymbol{e}^{e,A}+\Delta\boldsymbol{e}\| - \sqrt{\frac{2}{3}}d\left(\varepsilon_{s}^{p}\right)}{2G - \frac{4}{3}\frac{s_{us,p}}{\varepsilon_{s,r}^{p}}} \end{aligned} \tag{29}$$

Alternatively, it can be determined by forcing the deviatoric stress at state *B* (q^{B}) to fall at the reduced yield surface, by

$$q^B = q^T - 3G\Delta\varepsilon_s^p = d\left(\varepsilon_s^p\right) - \frac{\Delta\varepsilon_s^p}{\varepsilon_{s,r}^p} 2s_{u,p} \rightarrow \Delta\varepsilon_s^p = \frac{q^T - d\left(\varepsilon_s^p\right)}{3G - 2\frac{s_{u,p}}{\varepsilon_{s,r}^p}} \tag{30}$$

where $q^T = 2\sqrt{\frac{3}{2}} G \left\| \boldsymbol{e^A} + \Delta \boldsymbol{e} \right\|$ is the deviatoric stress at the virtual state *T*. The elastic strain tensor at the new state *B* is therefore

$$\boldsymbol{e}^{e,B} = \left(\mathbf{1} - \frac{\|\Delta \boldsymbol{e}^p\|}{\|\boldsymbol{e^A} + \Delta \boldsymbol{e}\|} \right) (\boldsymbol{e}^{e,A} + \Delta \boldsymbol{e}) \tag{31}$$

The stress tensors can then be fully solved through equations (23) to (26).

Non-negative value of incremental plastic strain requires

$$2G - \frac{4}{3} \frac{s_{us,p}}{\varepsilon_{s,r}^p} > 0 \rightarrow s_{us,p} < \frac{3}{2} G \varepsilon_{s,r}^p \tag{32}$$

The physical meaning of inequality (32) is that the softening rate $\frac{s_{\mathrm{u,p}}}{\gamma_{\mathrm{r}}^{\mathrm{p}}}$ should be less than the unloading shear modulus; otherwise, the portion of plastic shear strain transferred from the initially elastic part (due to softening) may self-drive the softening process. Therefore, if inequality (32) is not satisfied, the shear strength would be essentially reduced to the residual even with little plastic deformation.

Shear stress at weak layer

Within the slip surface, the shear stress (τ_{w}) is limited to the current shear strength, which is reduced during shearing, and given by

$$\tau_w = s_{uw}(\delta^p) = max\left(1 - \frac{\delta^p}{\delta_r^p}, \quad \frac{1}{S_t}\right) \cdot s_{uw,p} \tag{33}$$

where $\delta^{\mathrm{p}} = \int_0^t \left\| \dot{\boldsymbol{\delta}}^{\mathrm{p}} \right\| dt$ is the accumulated plastic shear displacement across the weak layer, $\delta_{\mathrm{r}}^{\mathrm{p}}$ the value of δ^{p} at the residual shear stress, and $s_{\mathrm{uw,p}}$ the peak undrained shear strength in the weak layer. Ignoring displacement beneath the weak layer (Zhang et al. 2015), the horizontal slide displacement can be related to the shear displacement across the weak layer by $\frac{u}{\cos\theta} =$

$\delta = \delta^{\mathrm{e}} + \delta^{\mathrm{p}}$ where θ is the slope angle and δ^{e} and δ^{p} the elastic and plastic portion of the shear displacement, respectively.

Soils surrounding the slip surface are first mobilized elastically before reaching the yield stress governed by equation (27), and the shear stress is increased to be larger than the initial value caused by gravity. Considering a linear and isotropic elasticity model, the pre-peak shear stress can be expressed by

$$\boldsymbol{\tau}_w = K\boldsymbol{\delta}^e \tag{34}$$

where K is the shear stiffness.

Figure A1b gives details of the constitutive model for weak layer soils in the $\tau_{\mathrm{w},x} - \tau_{\mathrm{w},y}$ plane, where the strain softening behaviour is isotropic, i.e., reduction of shear strength in the *x*-axis results in the same-magnitude reduction in the *y*-axis. Similar to equation (29), the incremental plastic shear displacement can be given by

$$\begin{aligned} K\|\boldsymbol{\delta}^{e,A} + \Delta\boldsymbol{\delta}\| - K\|\Delta\boldsymbol{\delta}^{p}\| = s_{uw}(\delta^{p}) - \frac{s_{uw,p}}{\delta_r^{p}}\|\Delta\boldsymbol{\delta}^{p}\| \rightarrow \|\Delta\boldsymbol{\delta}^{p}\| \\ = \frac{K\|\boldsymbol{\delta}^{e,A} + \Delta\boldsymbol{\delta}\| - s_{uw}(\delta^{p})}{K - \frac{s_{uw,p}}{\delta_r^{p}}} \end{aligned} \tag{35}$$

Again, a non-negative value of $\|\Delta\boldsymbol{\delta}^{\mathrm{p}}\|$ requires

$$K - \frac{s_{uw,p}}{\delta_r^{p}} > 0 \rightarrow s_{uw,p} < K\delta_r^{p} \tag{36}$$

Otherwise, the shear strength could be immediately reduced to the residual upon any small plastic deformation.

The updated elastic shear displacement is therefore

$$\boldsymbol{\delta}^{e,B} = \left(1 - \frac{\|\Delta\boldsymbol{\delta}^{p}\|}{\|\boldsymbol{\delta}^{e,A} + \Delta\boldsymbol{\delta}\|}\right)(\boldsymbol{\delta}^{e,A} + \Delta\boldsymbol{\delta}) \tag{37}$$

797 and the weak layer stress (vector) can then be updated through equation (34).

798 ***Gravity and drag shear stresses***

799 The gravity shear stress is given by

$$\tau_g = \gamma' h \sin\theta \tag{38}$$

800 where γ' is the submerged unit weight of soil.

801 Hydrodynamic pressure drag for a streamlined body like a submarine sliding mass is less
802 significant than the skin friction drag, and the latter can be approximated by (Norem et al. 1990,
803 Elverhoi et al. 2005)

$$\tau_{drag} = \frac{1}{2} C_f \rho_w v^2;\ C_f = \left(1.89 + 1.62\, log\frac{L}{k}\right)^{-2.5} \tag{39}$$

804 where C_f is the frictional drag coefficient, ρ_w is the seawater density, L is the sliding mass
805 length and k is the roughness length of the sliding mass surface in the range of 0.01–0.1 m. For
806 a length of the sliding mass varying between 10 and 1000 m, the friction drag coefficient falls
807 in the range of 0.005–0.016.

808 ***Finite volume scheme***

809 Two layers of fixed meshes with the same mesh size and alignment were taken, as shown in
810 Figure A2a, with the top layer used for solving mass and momentum conservation equations
811 and the bottom layer tracking the changes in soil properties in the weak layer during slip surface
812 growth. A finite volume method with staggered grids, as shown in Figure A2b, was used to
813 integrate and solve the governing equations (1) to (3).

814 Let us consider a slope of a rectangular space domain Ω: $(0, L_x) \times \left(0, L_y\right)$ and a time interval
815 $(0, T)$. Dirichlet boundary conditions, i.e., $u = 0$ and $v = 0$, are prescribed representing

unaffected remote regions. The space domain is meshed with a grid of $N_x \times N_y$ cells, and the cells of dimensions Δx and Δy are indexed by (i,j) where $i \in (0, N_x)$ and $i \in \left(0, N_y\right)$. The centres of the bottom, top, left, and right edges of the cell (i,j) are denoted by $\left(i, j-\frac{1}{2}\right)$, $\left(i, j+\frac{1}{2}\right)$, $\left(i-\frac{1}{2}, j\right)$, and $\left(i+\frac{1}{2}, j\right)$, respectively. The mass conservation is integrated and solved over the cell, with the thickness of the sliding layer, h, and slope angle (topography), θ, discretised at the cell centre. The velocity in the *x*-direction is discretised at the centre of the edges normal to the *x*-direction, while the velocity in the *y*-direction is discretised at the centre of the edges normal to the *y*-direction. The approximation of h at cell (i,j) and time t^n is denoted by $h_{i,j}^n$. The approximation of u at the edge $\left(i+\frac{1}{2}, j\right)$ and time t^n is denoted by $u_{i+\frac{1}{2},j}^n$ while the approximation of v at the edge $\left(i, j+\frac{1}{2}\right)$ and time t^n is denoted $v_{i,j+\frac{1}{2}}^n$.

At time t^{n+1}, the mass conservation equation (1) is discretised as

$$h_{i,j}^{n+1} - h_{i,j}^n = \frac{\Delta t}{\Delta x}\left(qx_{i-\frac{1}{2},j}^n - qx_{i+\frac{1}{2},j}^n\right) + \frac{\Delta t}{\Delta y}\left(qy_{i-\frac{1}{2},j}^n - qy_{i+\frac{1}{2},j}^n\right) \tag{40}$$

where

$$\begin{aligned} qx_{i-\frac{1}{2},j}^n &= \hat{h}_{i-\frac{1}{2},j}^n u_{i-\frac{1}{2},j}^n, \hat{h}_{i-\frac{1}{2},j}^n = \begin{cases} h_{i,j}^n & u_{i-\frac{1}{2},j}^n \le 0 \\ h_{i-1,j}^n & u_{i-\frac{1}{2},j}^n > 0 \end{cases}; \\ qy_{i,j-\frac{1}{2}}^n &= \hat{h}_{i,j-\frac{1}{2}}^n v_{i,j-\frac{1}{2}}^n, \hat{h}_{i,j-\frac{1}{2}}^n = \begin{cases} h_{i,j}^n & v_{i,j-\frac{1}{2}}^n \le 0 \\ h_{i,j-1}^n & v_{i,j-\frac{1}{2}}^n > 0 \end{cases} \end{aligned} \tag{41}$$

The momentum conservation in the *x*-direction, i.e., equation (2), is discretised as

$$
\begin{aligned}
&h^{n+1}_{i+\frac{1}{2},j}u^{n+1}_{i+\frac{1}{2},j} - h^{n}_{i+\frac{1}{2},j}u^{n}_{i+\frac{1}{2},j} \\
&\quad = \frac{\Delta t}{\Delta x}\left(qx^{n}_{i,j}\hat{u}^{n}_{i,j} - qx^{n}_{i+1,j}\hat{u}^{n}_{i+1,j}\right) \\
&\quad + \frac{\Delta t}{\Delta y}\left(qy^{n}_{i+\frac{1}{2},j-\frac{1}{2}}\hat{u}^{n}_{i+\frac{1}{2},j-\frac{1}{2}} - qy^{n}_{i+\frac{1}{2},j+\frac{1}{2}}\hat{u}^{n}_{i+\frac{1}{2},j+\frac{1}{2}}\right) \\
&\quad + \frac{\Delta t}{\rho\Delta y}\left(\tau^{n}_{xy,i+\frac{1}{2},j+\frac{1}{2}}h^{n}_{i+\frac{1}{2},j+\frac{1}{2}} - \tau^{n}_{xy,i+\frac{1}{2},j-\frac{1}{2}}h^{n}_{i+\frac{1}{2},j-\frac{1}{2}}\right) \\
&\quad + \frac{\tau^{n}_{w,i+\frac{1}{2},j} + \tau^{n}_{g,i+\frac{1}{2},j} + \tau^{n}_{drag,i+\frac{1}{2},j}}{\rho}
\end{aligned}
\tag{42}
$$

where

$$
h^{n}_{i+\frac{1}{2},j} = \frac{h^{n}_{i,j} + h^{n}_{i+1,j}}{2};
$$

$$
qx^{n}_{i,j} = \frac{qx^{n}_{i-\frac{1}{2},j} + qx^{n}_{i+\frac{1}{2},j}}{2},\ \hat{u}^{n}_{i,j} = \begin{cases} u^{n}_{i+\frac{1}{2},j} & qx^{n}_{i,j} \le 0 \\ u^{n}_{i-\frac{1}{2},j} & qx^{n}_{i,j} > 0 \end{cases};
$$

$$
qy^{n}_{i+\frac{1}{2},j-\frac{1}{2}} = \frac{qy^{n}_{i,j-\frac{1}{2}} + qy^{n}_{i+1,j-\frac{1}{2}}}{2},\ \hat{u}^{n}_{i+\frac{1}{2},j-\frac{1}{2}} = \begin{cases} u^{n}_{i+\frac{1}{2},j} & qy^{n}_{i+\frac{1}{2},j-\frac{1}{2}} \le 0 \\ u^{n}_{i+\frac{1}{2},j-1} & qy^{n}_{i+\frac{1}{2},j-\frac{1}{2}} > 0 \end{cases};
\tag{43}
$$

$$
\begin{aligned}
&\tau^{n}_{xy,i+\frac{1}{2},j+\frac{1}{2}}h^{n}_{i+\frac{1}{2},j+\frac{1}{2}} \\
&\quad = \frac{\tau^{n}_{xy,i,j}h^{n}_{i,j} + \tau^{n}_{xy,i+1,j}h^{n}_{i+1,j} + \tau^{n}_{xy,i,j+1}h^{n}_{i,j+1} + \tau^{n}_{xy,i+1,j+1}h^{n}_{i+1,j+1}}{4}
\end{aligned}
$$

The momentum conservation in the *y*-direction, i.e., equation (3), can be discretised in a similar way.

833

834

835 **List of tables**

839

840

841 Table 1 Parameters for benchmark case

Parameter	Value	Unit
Length of slope	8,000	m
Maximum slope angle, θ_c	6	degrees
Half slope height, H	20	m
Shear modulus, G	662.25	kPa
Shear stiffness in the weak layer, K	1656	kPa/m
At-rest earth pressure coefficient, K_0	0.75	
Gravity acceleration, g	9.81	m/s^2
Saturated density, ρ	1870	kg/m^3
Peak undrained shear strength in weak layer, $s_{uw,p}$	10	kPa
Peak undrained shear strength in sliding layer, $s_{us,p}$	10, 20, 30, 100	kPa
Soil sensitivity in weak layer	5	
Soil sensitivity in sliding layer	1	
Residual plastic shear displacement, δ_r^p	0.2	m

842

843

844 Table 2 Base parameters for numerical cases

Parameter	**Value**	**Unit**
Overall model length, L	4,000	m
Overall model width, B	150	m
Slope angle, θ	6.0	degrees
Sliding layer thickness, h	8.0	m
Shear stiffness in weak layer, K	1,656	kPa/m
Shear modulus in sliding layer, G	500	kPa
Peak shear strength in weak layer, $s_{uw,p}$	10	kPa
Residual shear strength in weak layer, $s_{uw,r}$	2	kPa
Plastic shear displacement to the residual strength, δ_r^p	0.2	m
Plastic shear strain to the residual strength, $\varepsilon_{s,r}^p$	0.2	
At-rest lateral earth pressure coefficient, K_0	0.5	
Characteristic length[1], l_c	10	m
Submerged soil density, ρ	740	kg/m^3

845 [1] $l_{\mathrm{c}} = \sqrt{\frac{Gh\delta_{\mathrm{r}}^{\mathrm{p}}}{\tau_{\mathrm{p}} - \tau_{\mathrm{r}}}}$

846

847

848 Table 3 Critical conditions for unstable slip surface growth by numerical analysis

Dimension of slip surface				**Gravity load**	
l_x **(m)**	l_y **(m)**	n	A **(m²)**	ρ **(kg/m³)**	r
First series: $l_y/l_x = 1$, $n = 2$					
10	10	2	79	1,170	0.943
20	20	2	314	1,070	0.841
40	40	2	1,257	870	0.637
60	60	2	2,827	730	0.494
80	80	2	5,027	640	0.403
100	100	2	7,854	580	0.341
120	120	2	11,310	540	0.301
140	140	2	15,394	500	0.260
160	160	2	20,106	470	0.229
180	180	2	25,447	450	0.209
200	200	2	31,416	430	0.189
Second series: $l_y/l_x = 2$, $n = 2$					
10	20	2	157	1,130	0.902
20	40	2	628	980	0.749
40	80	2	2,513	750	0.515
60	120	2	5,655	630	0.392
80	160	2	10,053	550	0.311
100	200	2	15,708	500	0.260
120	240	2	22,619	460	0.219
140	280	2	30,788	430	0.189
Third series: $l_y/l_x = 3$, $n = 2$					
10	30	2	236	1,090	0.862
20	60	2	942	910	0.678
40	120	2	3,770	680	0.443
60	180	2	8,482	570	0.331
80	240	2	15,080	500	0.260
100	300	2	23,562	460	0.219
120	360	2	33,929	430	0.189
Fourth series: $l_y/l_x = 0.5$, $n = 2$					
20	10	2	157	1,130	0.902
40	20	2	628	990	0.760
80	40	2	2,513	770	0.535
120	60	2	5,655	640	0.403
160	80	2	10,053	560	0.321
200	100	2	15,708	510	0.270
240	120	2	22,619	470	0.229
280	140	2	30,788	450	0.209
Fifth series: $l_y/l_x = 2$, $n = 1$					
20	40	1	400	1,040	0.811
40	80	1	1,600	830	0.596
60	120	1	3,600	700	0.464
80	160	1	6,400	610	0.372
100	200	1	10,000	550	0.311
120	240	1	14,400	510	0.270
Sixth series: $l_y/l_x = 2$, $n = 10$					
20	40	10	789	950	0.719
40	80	10	3,154	720	0.484
60	120	10	7,097	590	0.352
80	160	10	12,617	520	0.280
100	200	10	19,715	470	0.229
120	240	10	28,389	440	0.199

849

List of figures

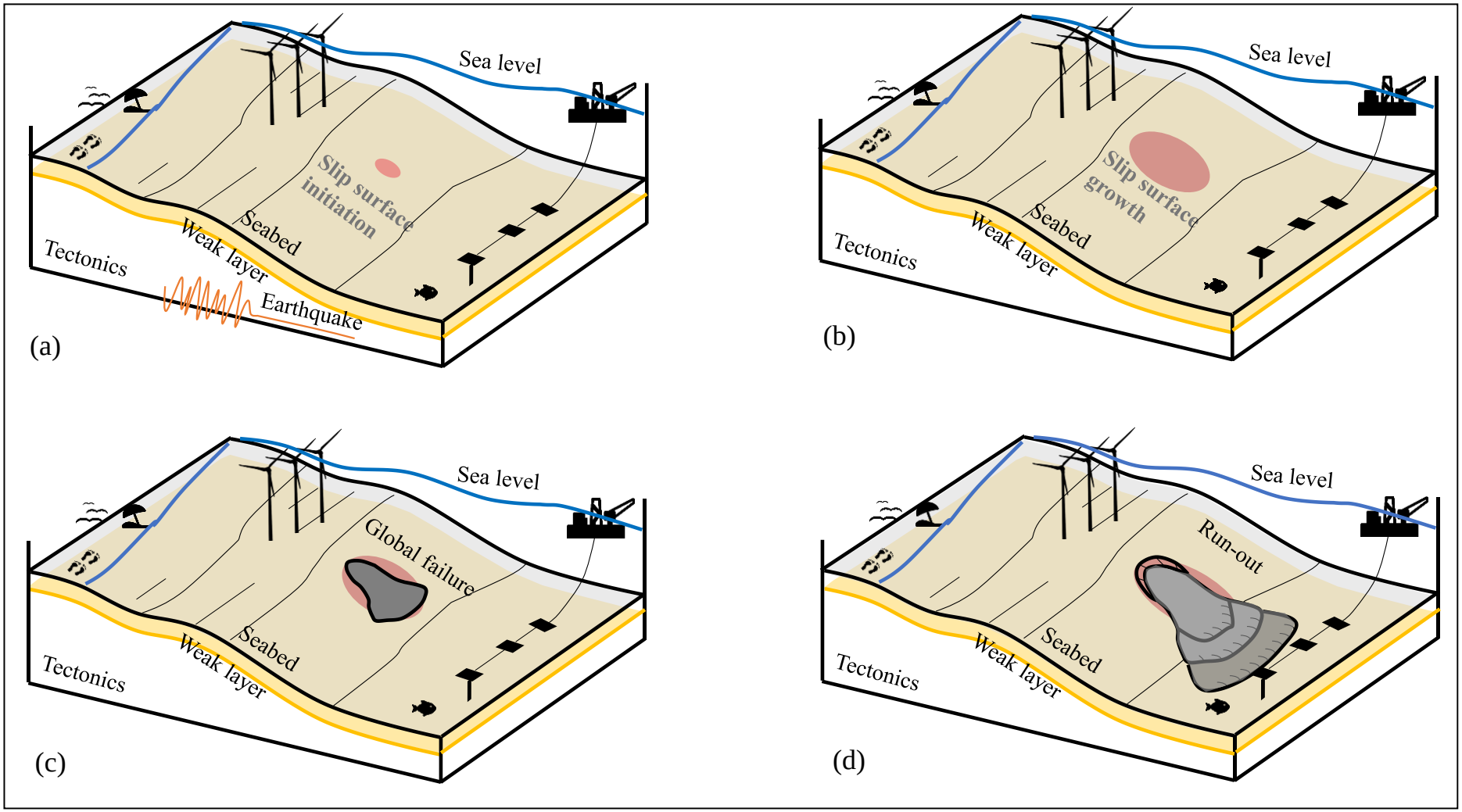

Figure 1 Conceptual evolution of submarine landslides: (a) local slip surface in weak layer; (b) slip surface growth; (c) global slab failure; (d) post-failure behaviour

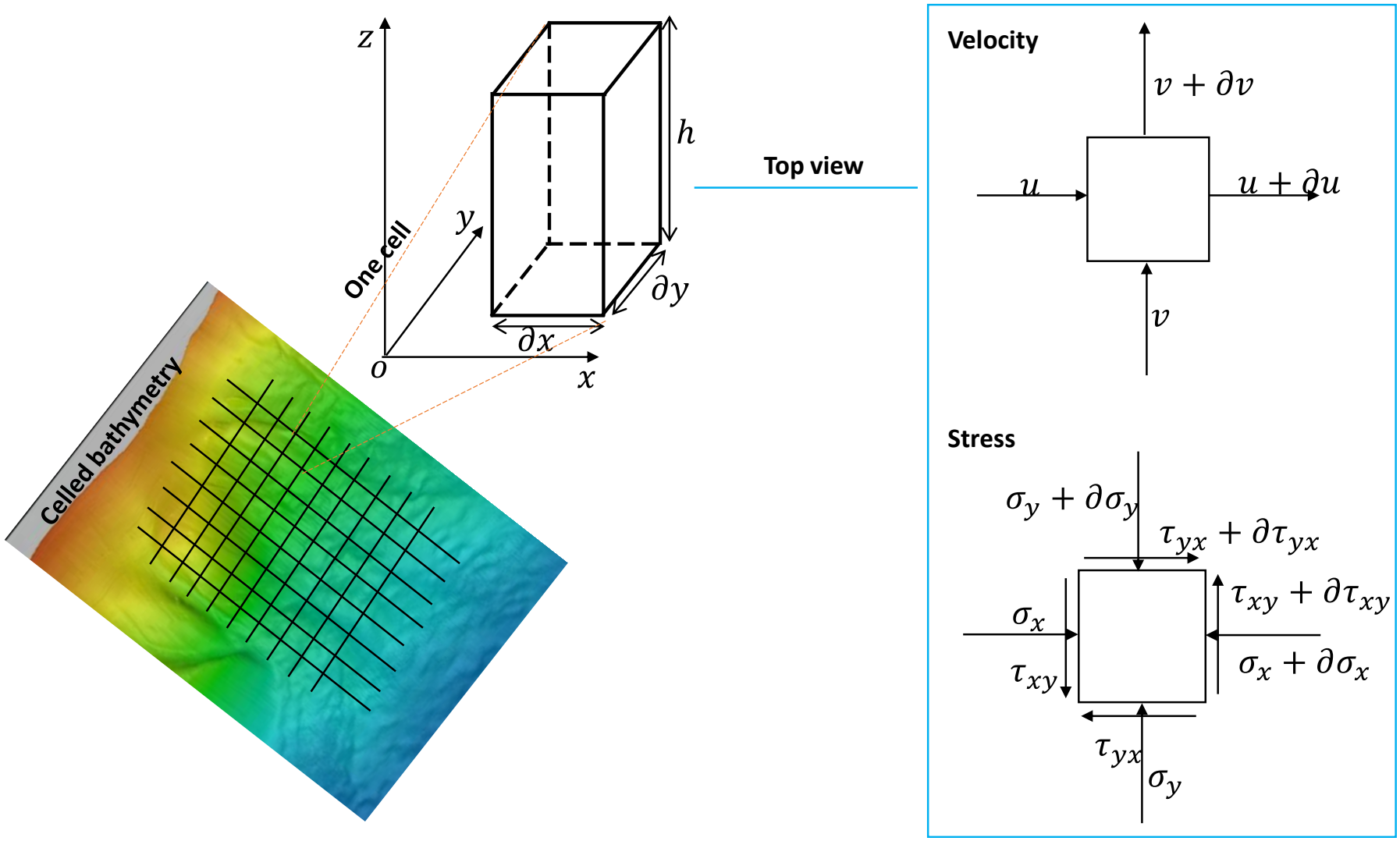

Figure 2 Discretisation and velocity and stress components of numerical model (bathymetry image shows the main scar of the Loch Eriboll Slide, after Carter et al. 2020)

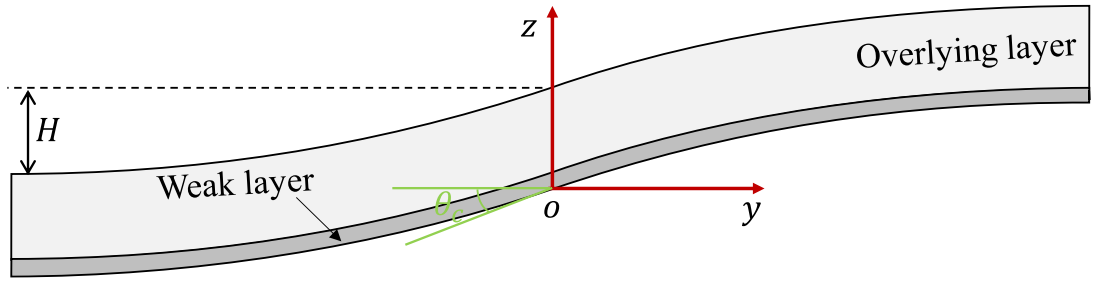

(a)

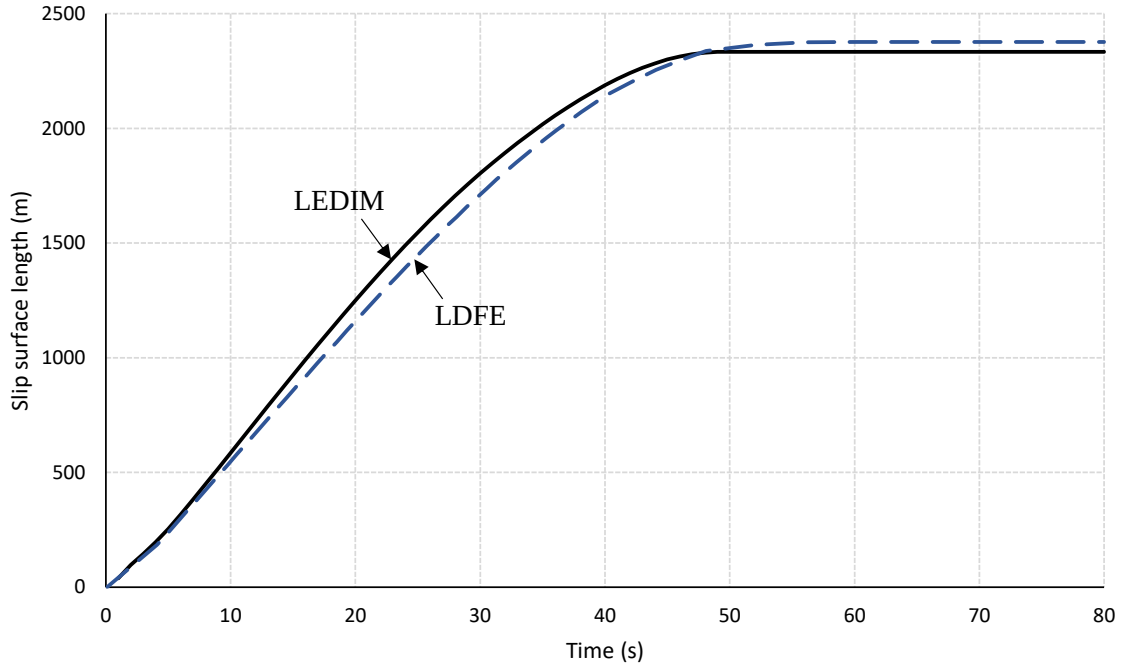

(b)

Figure 3 (a) Model used for verification case: 2D slope with 1D slip surface growth; (b) comparison of slip surface length obtained by large deformation finite element (LDFE) modelling and by the proposed depth integrated numerical scheme

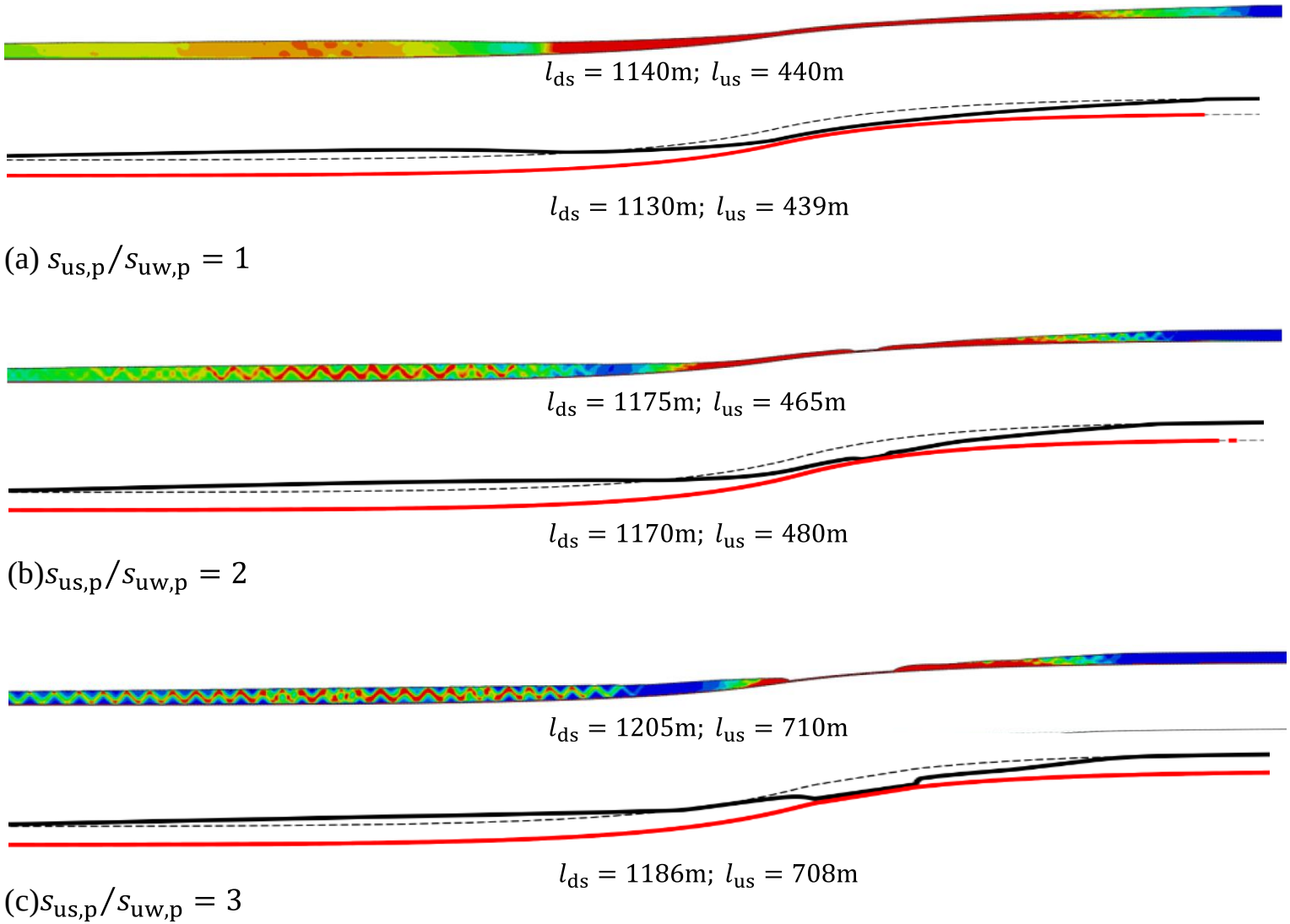

Figure 4 A comparison of two-dimensional post-failure configuration by large deformation finite element (LDFE) modelling and proposed depth integrated numerical scheme

907

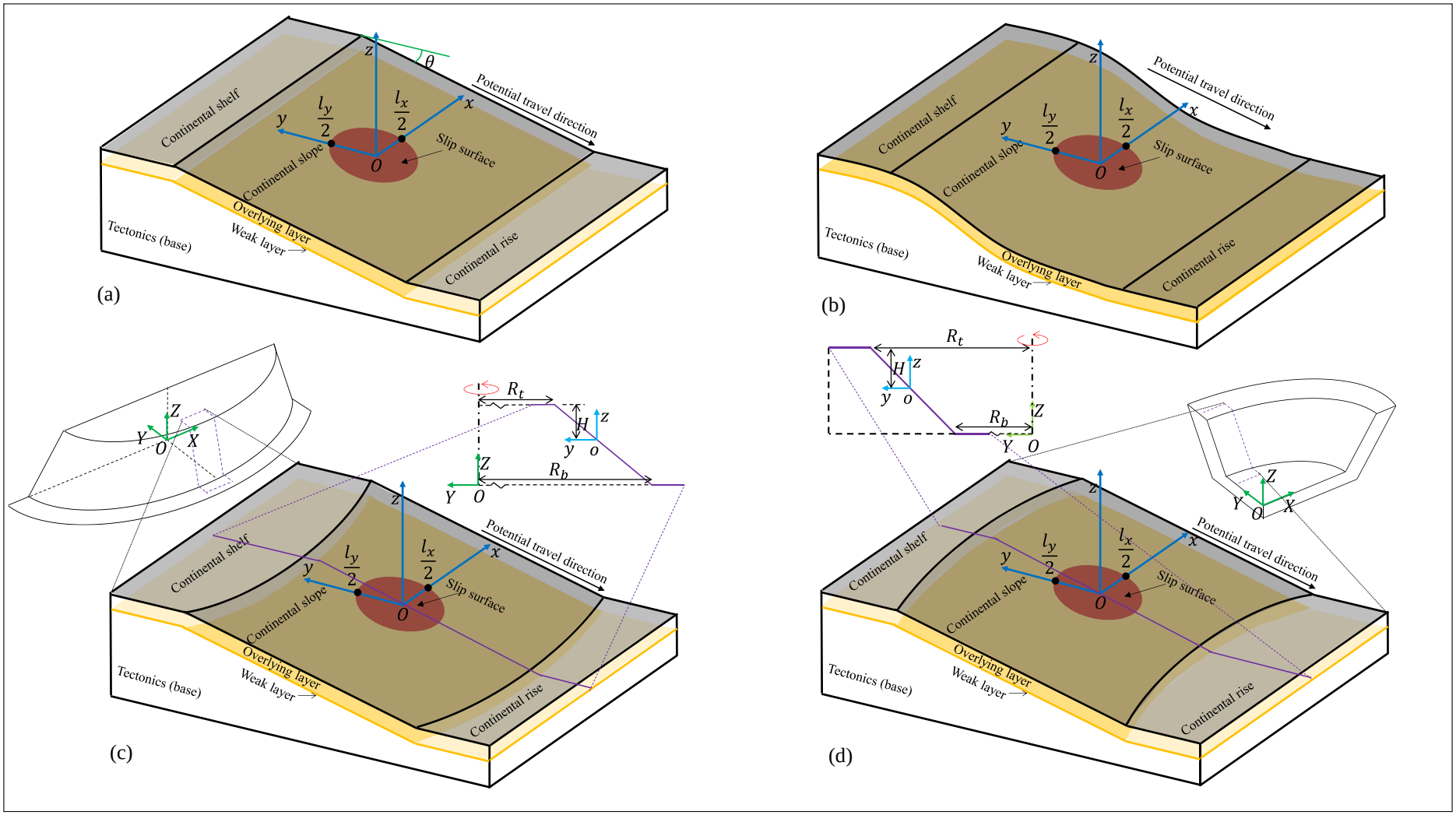

908

909 Figure 5 Conceptual 3D submarine slope models used in the study: (a) planar; (b) S-shape; (c) convex; and (d) concave

910

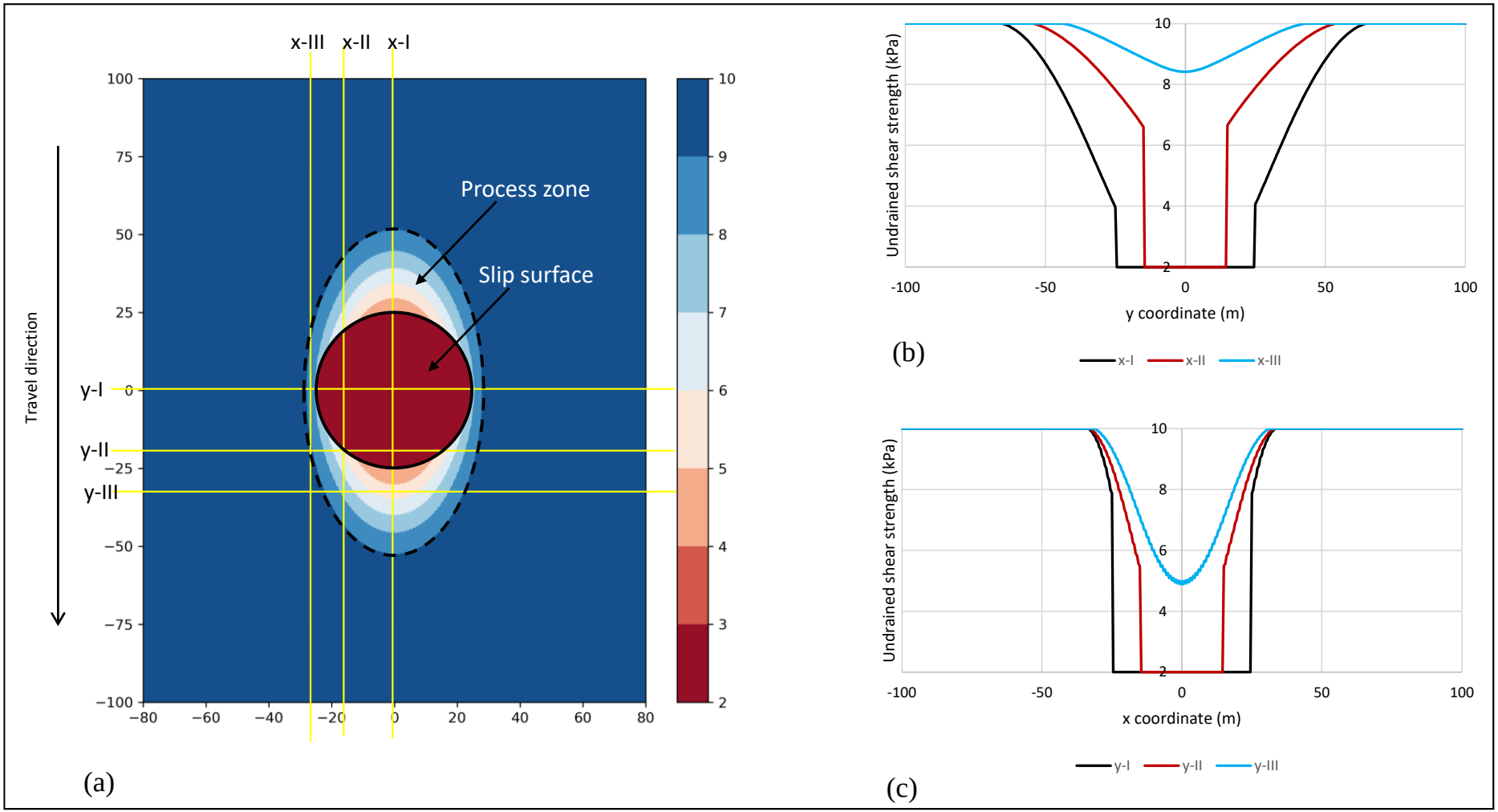

911

912 Figure 6 A typical case with stable growth of slip surface: (a) shear strength contour; (b) distributions of shear strength along cross sections
913 parallel to *x-axis*; and (c) distributions of shear strength along cross sections parallel to y-axis

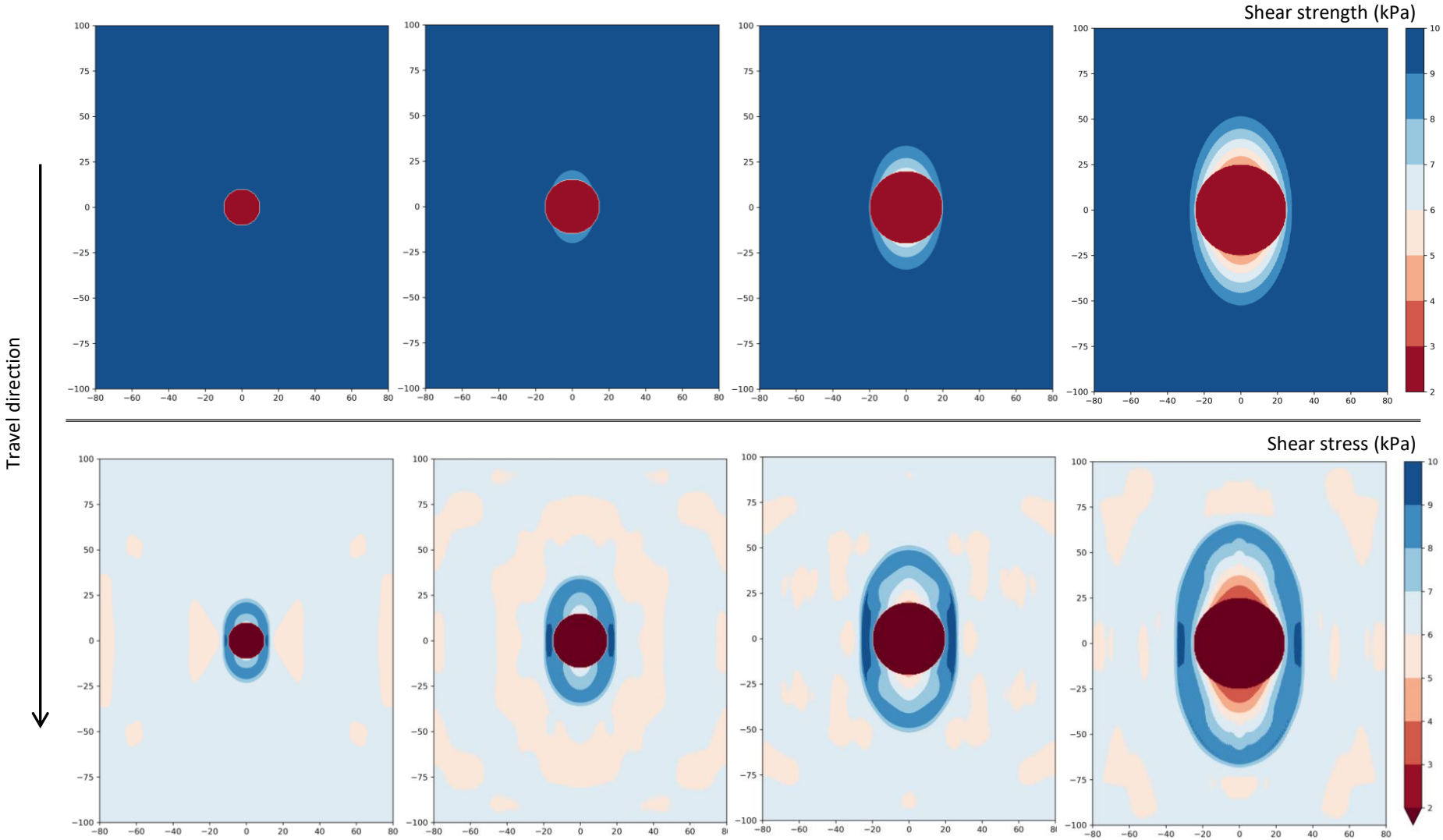

Figure 7 Evolution of shear strength (top row) and shear stress (bottom row) contours during stable growth of slip surface for a typical case

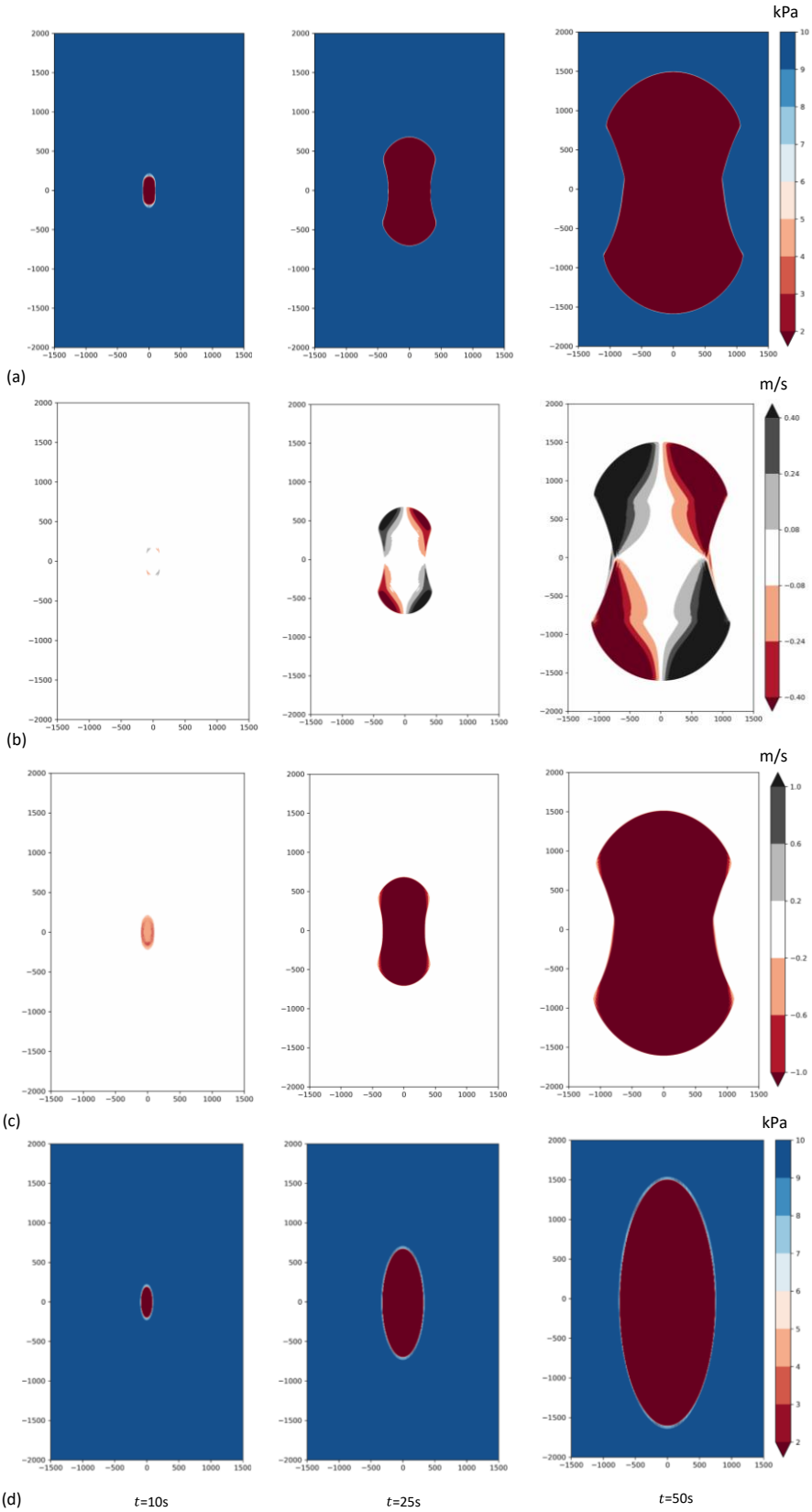

Figure 8 (a) Shear strength contours, (b) horizontal velocity contours and (c) vertical velocity contours for the case of free movement in *x* direction (perpendicular to the travel direction); and (d) shear strength contours for the case of restricted movement in *x* direction

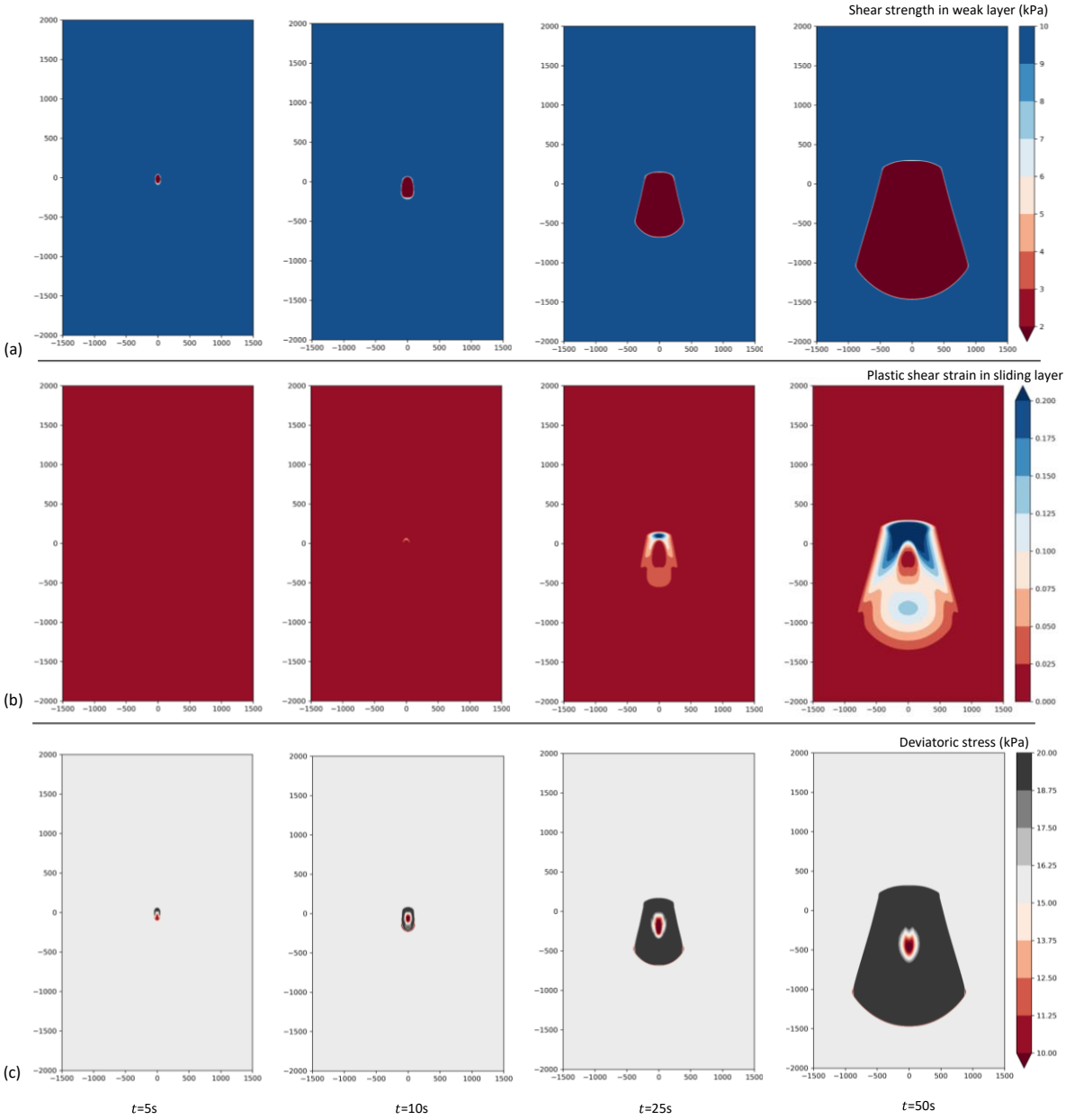

Figure 9 Contours of shear strength in weak layer and plastic shear strain in sliding layer for the case with $s_{\mathrm{us,p}}/s_{\mathrm{uw,p}} = 1$ and $K_0 = 0.5$

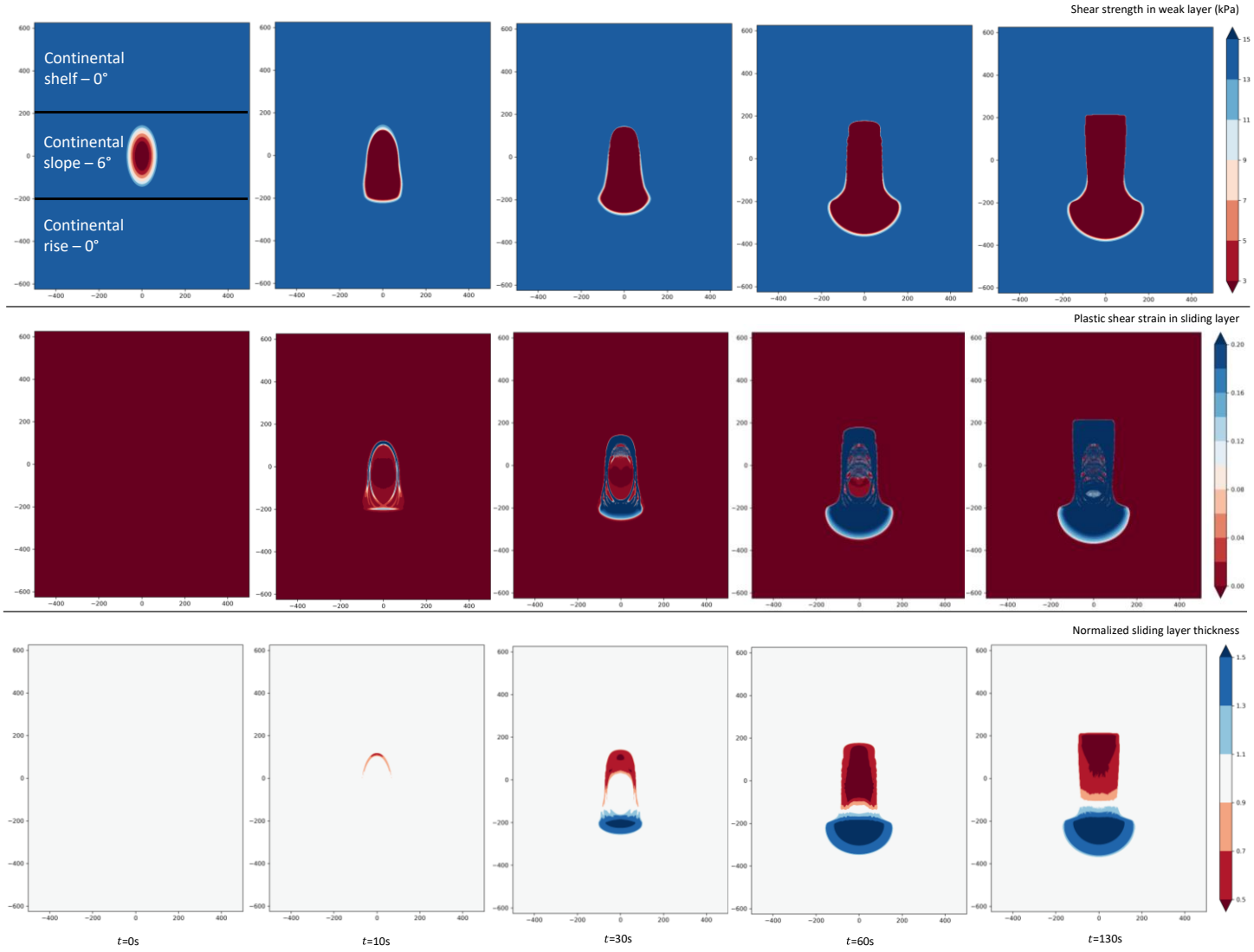
Shear strength in weak layer (kPa)
Continental shelf – 0°
Continental slope – 6°
Continental rise – 0°
Plastic shear strain in sliding layer
Normalized sliding layer thickness
t=0s
t=10s
t=30s
t=60s
t=130s

(a)

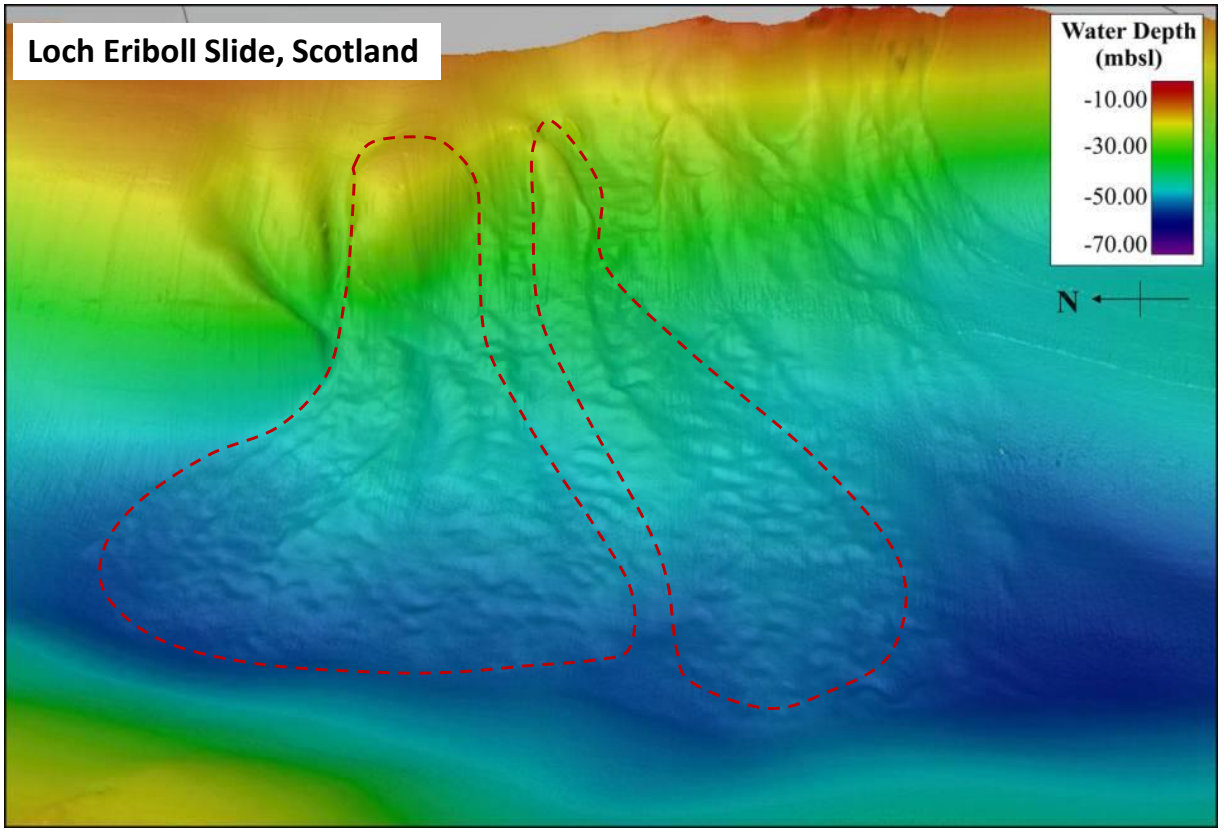

(b)

Figure 10 (a) Post-failure evolution of submarine landslides in terms of contours of shear strength in weak layer, plastic shear strain in sliding layer and normalised sliding layer thickness; (b) similar submarine landslide morphology discovered in the Loch Eriboll Slide (Carter et al. 2020)

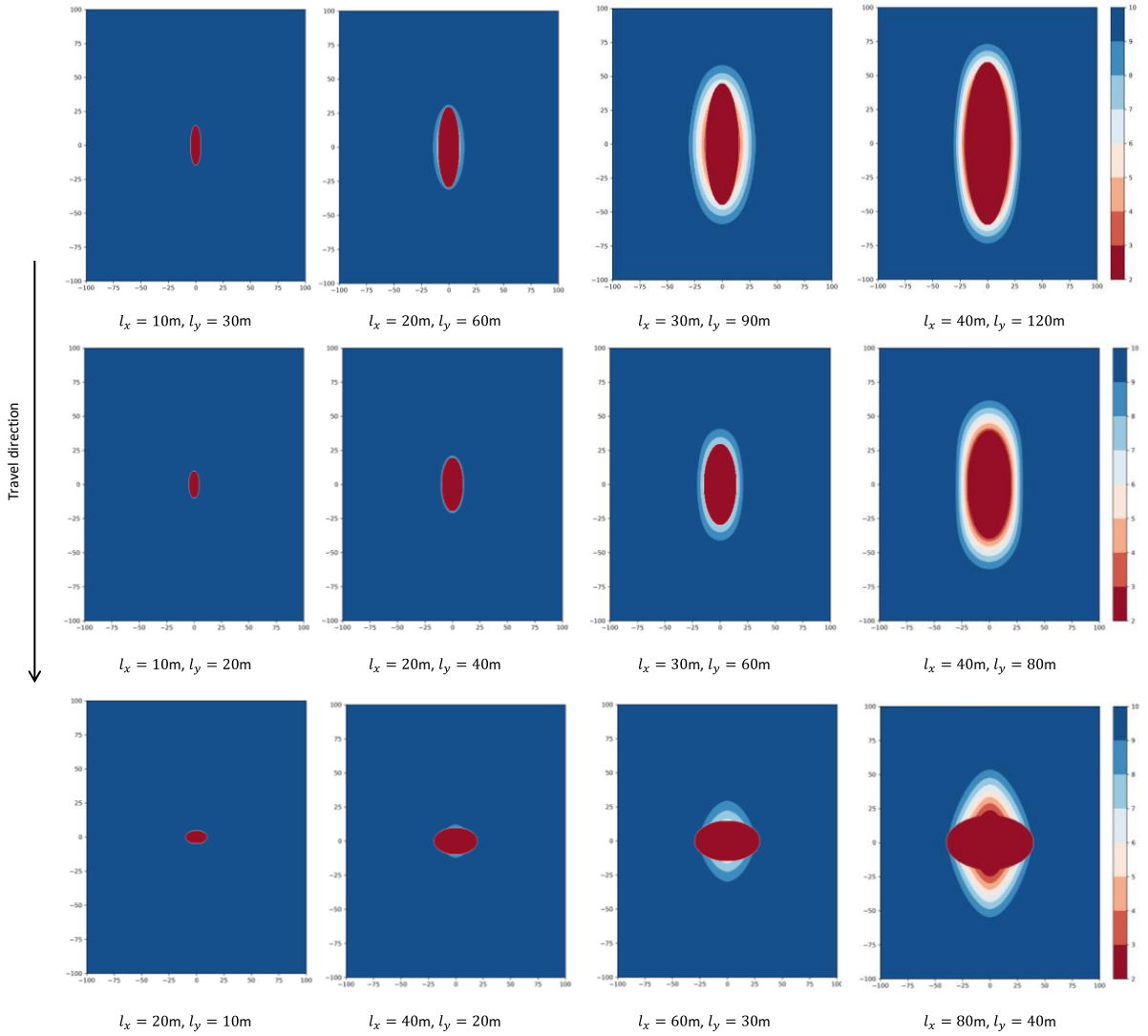

Figure 11 Stable growth of slip surface with different sizes and shapes of initiation zone

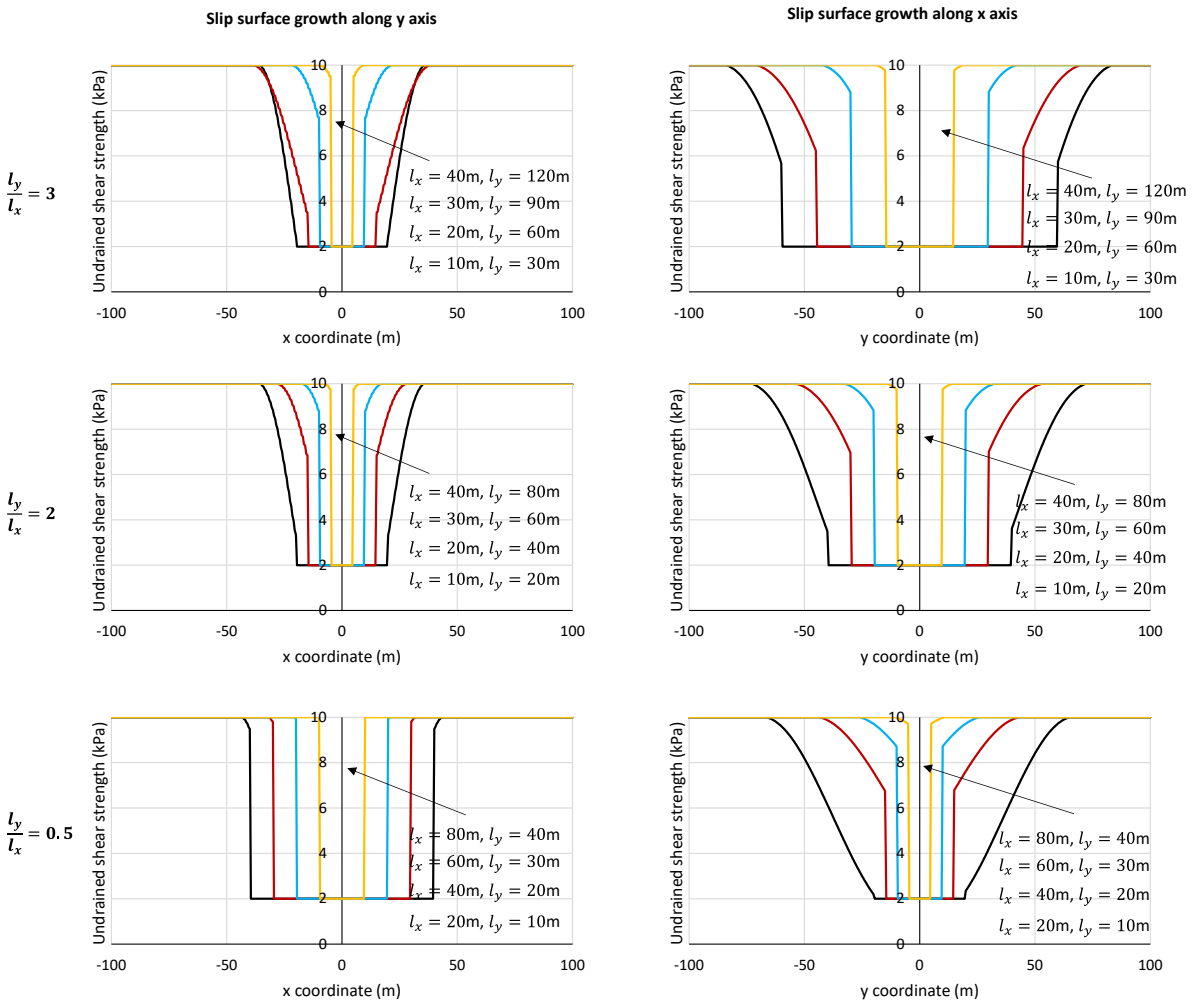

Figure 12 Distributions of shear strength along the *x*- and *y-axes during* stable growth of slip surface with different sizes and shapes

936

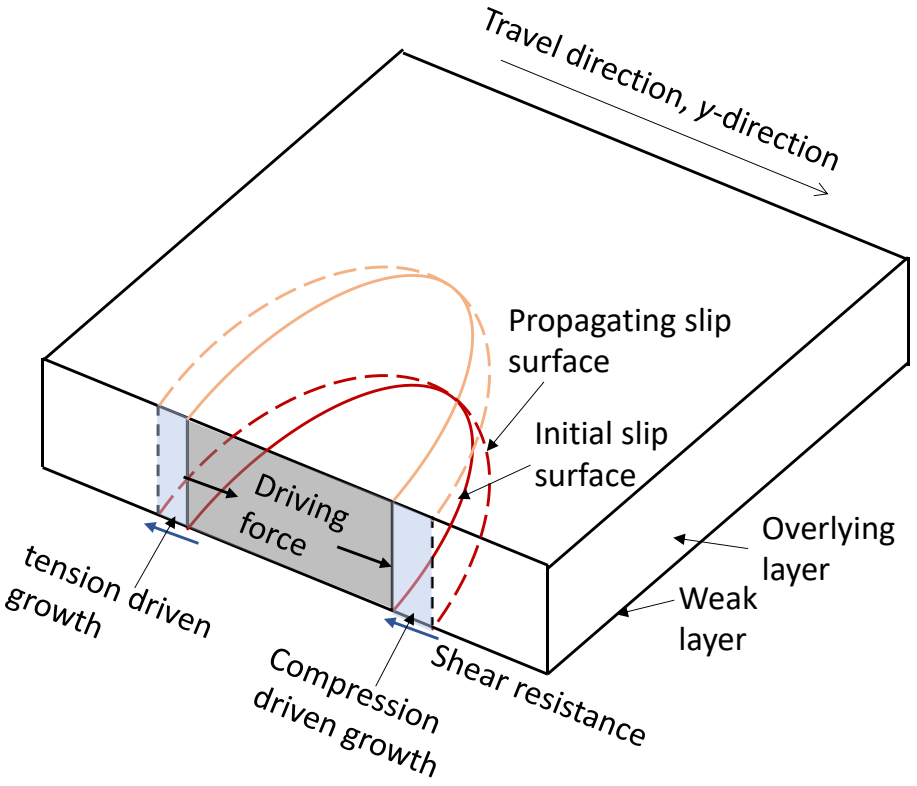

937

938 (a)

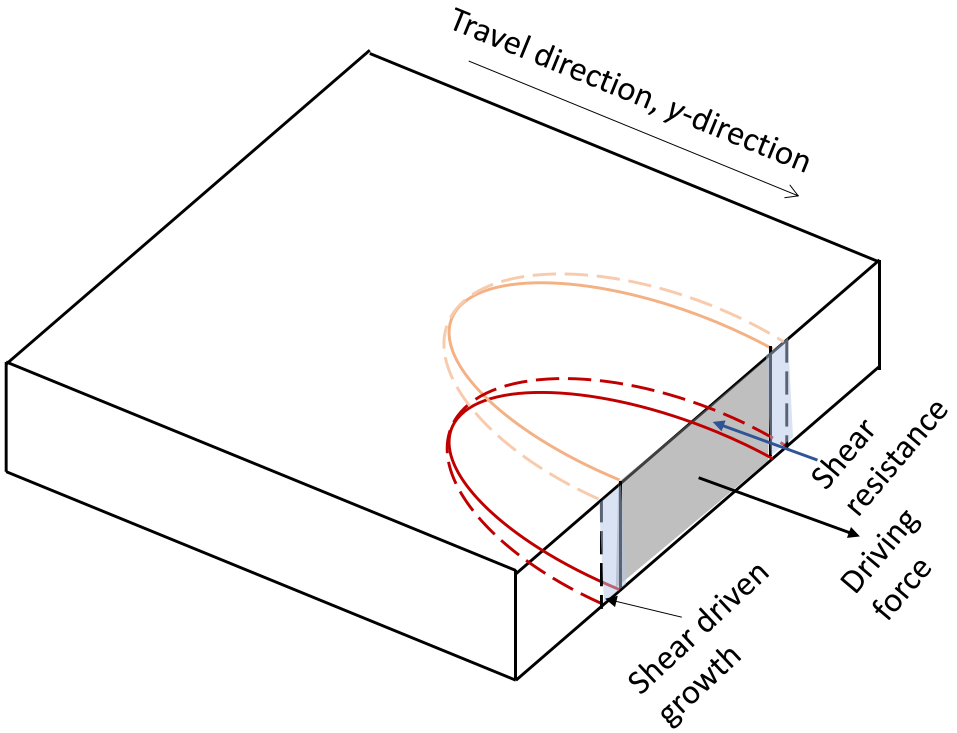

939

940 (b)

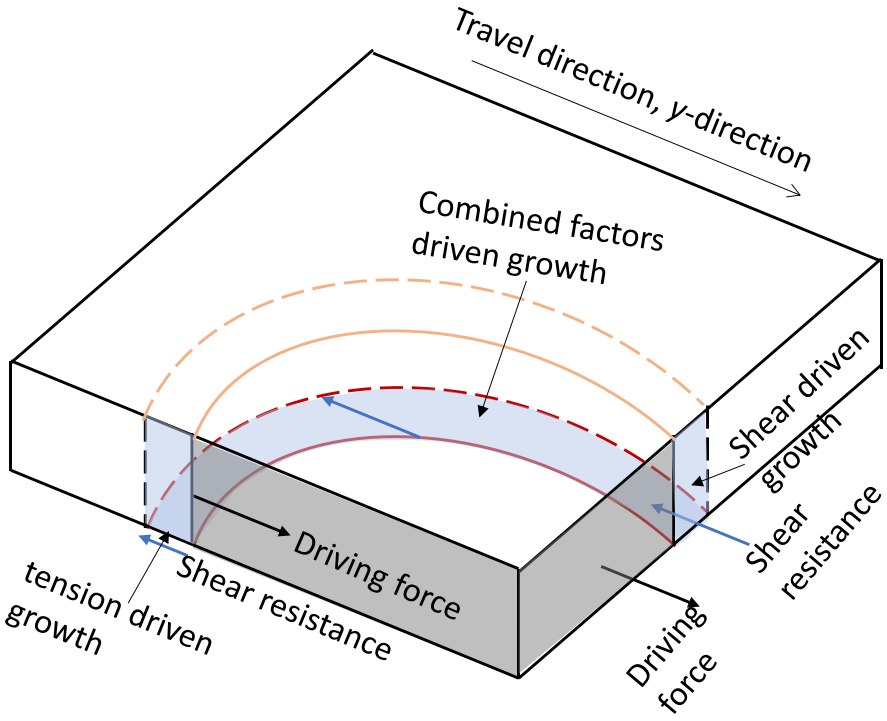

(c)

Figure 13 Three slip surface growth modes: (a) compression-extension mode; (b) shear mode; and (c) combined mode

946

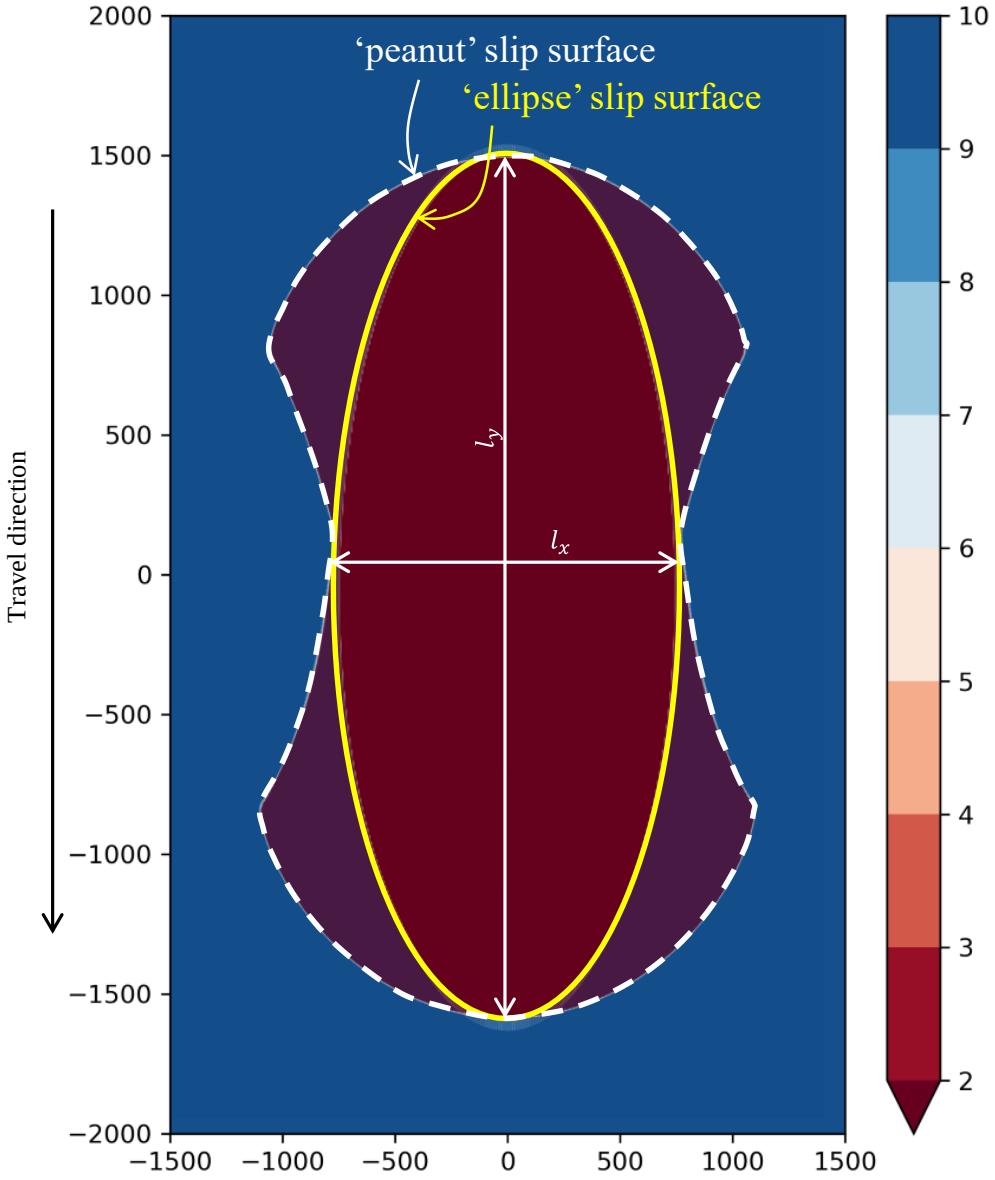

947

948 Figure 14 Two mechanisms for unstable growth of slip surface

949

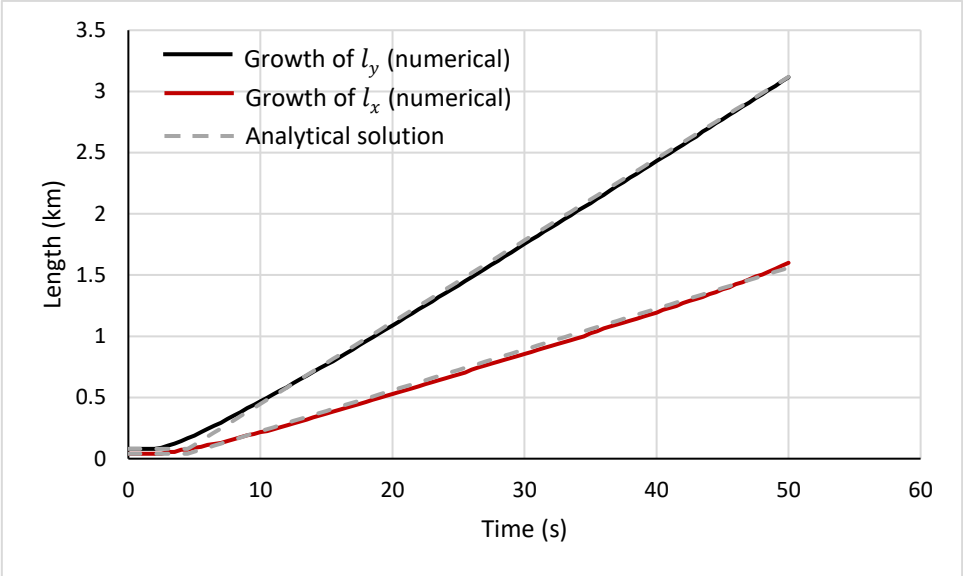

(a)

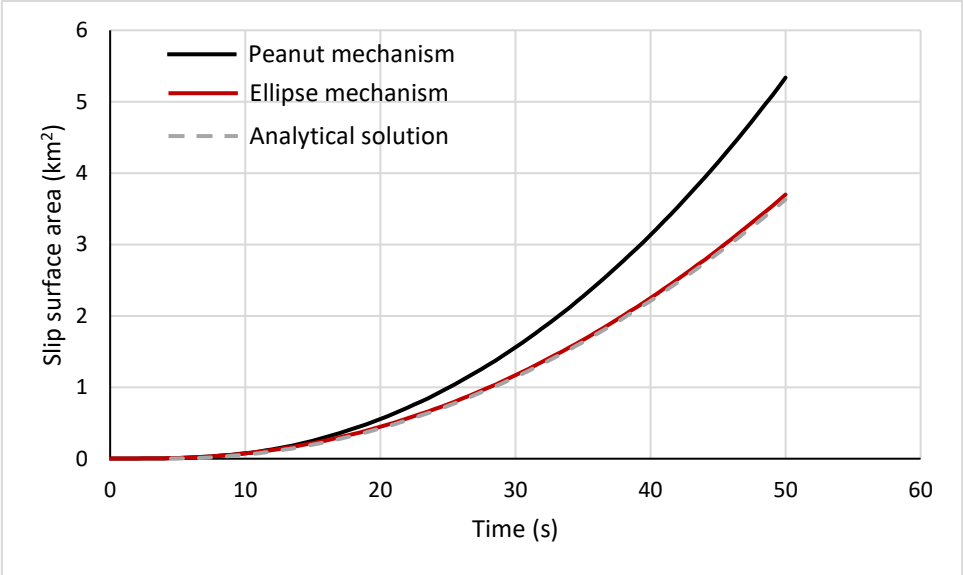

(b)

Figure 15 Speed of slip surface growth in terms of (a) major and minor axis lengths and (b) area of slip surface

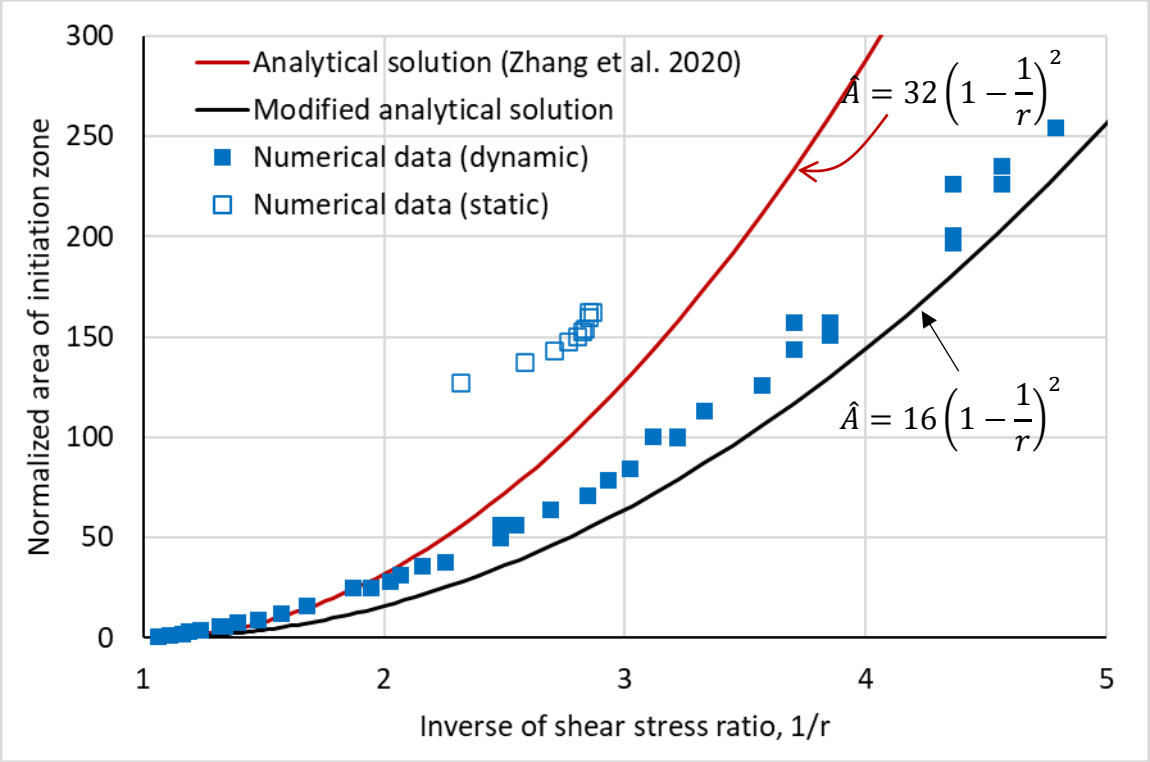

(a)

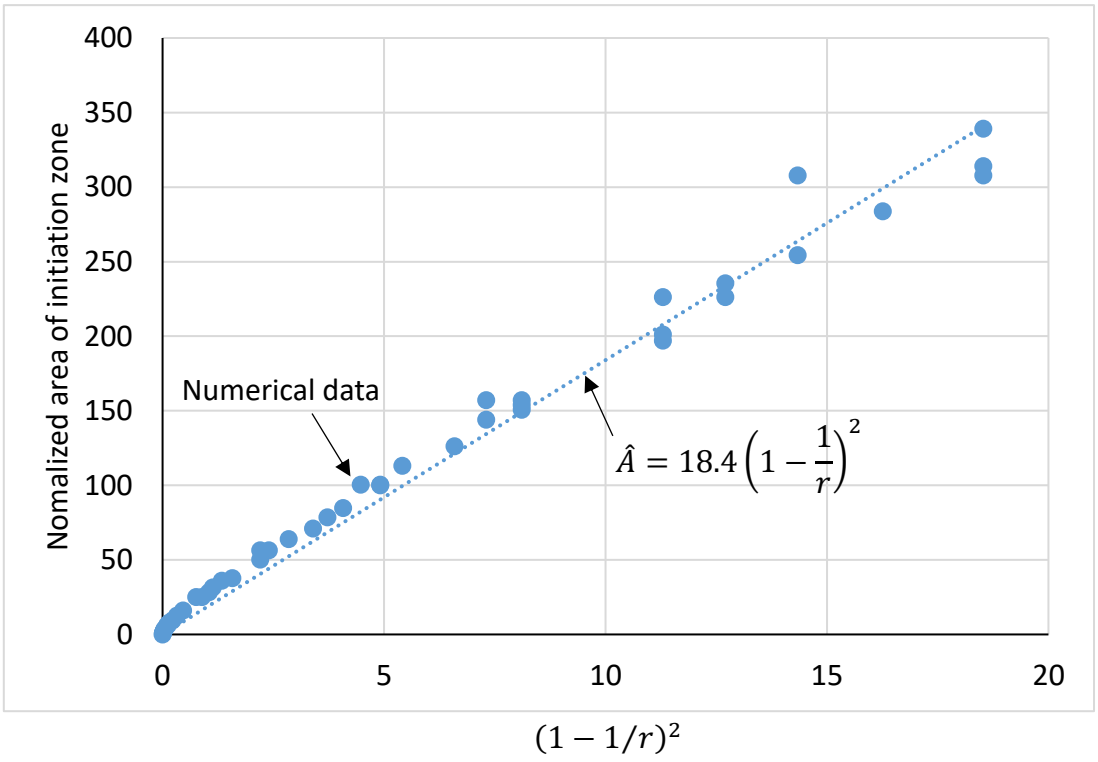

(b)

Figure 16 (a) Critical area of slip surface for unstable growth by numerical and analytical analyses; and (b) best fitting of numerical data

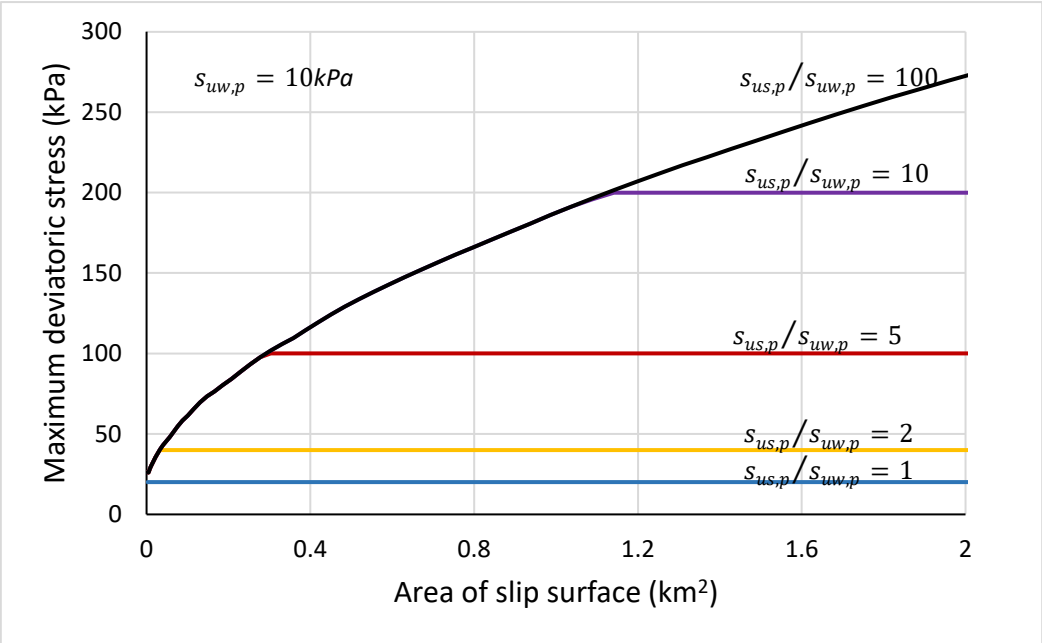

965

966 Figure 17 Maximum deviatoric stress in the sliding layer during unstable growth of slip

967 surface

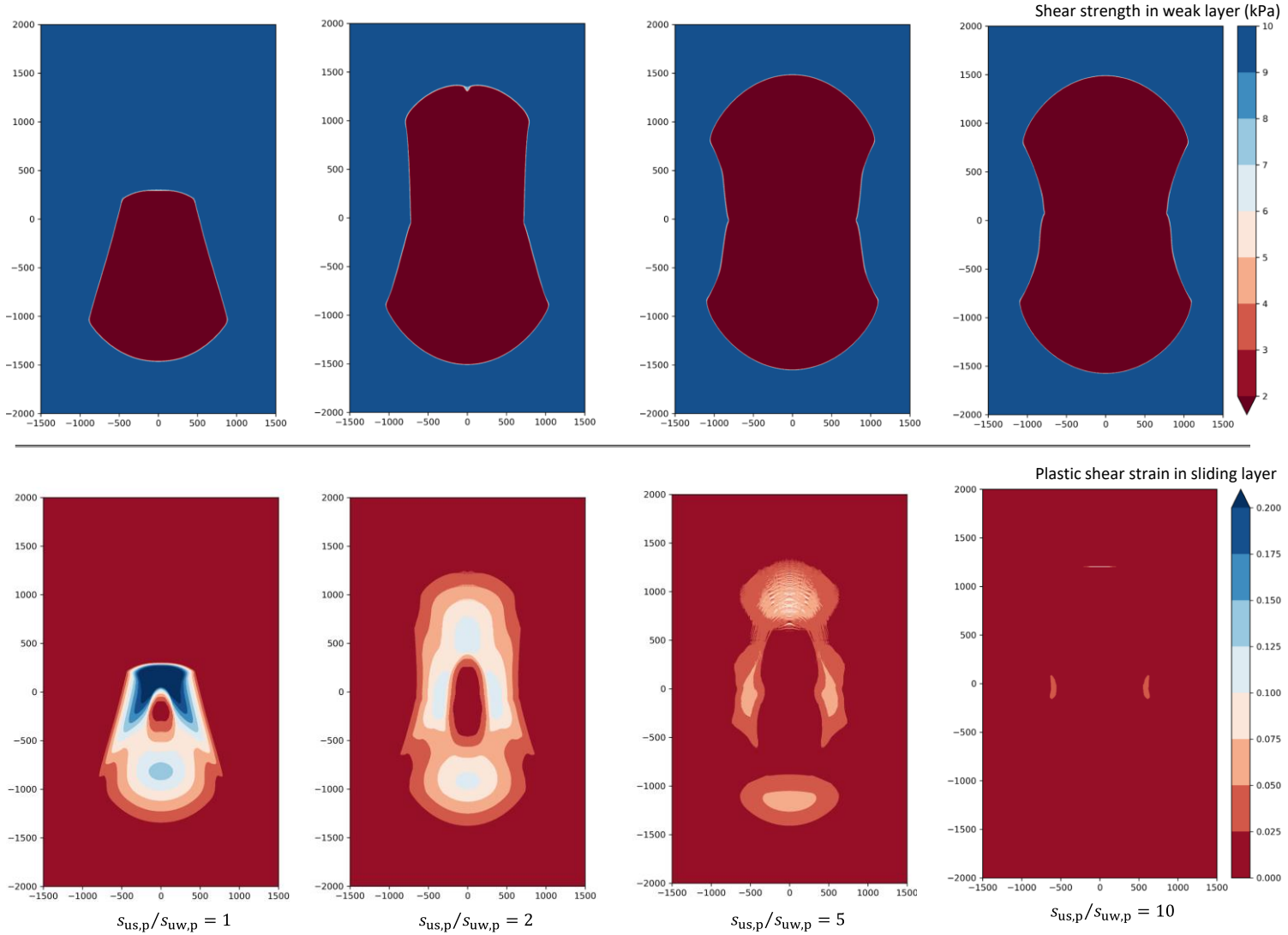

Figure 18 Contours of shear strength in weak layer and plastic shear strain in sliding layer for cases with different strength ratios $s_{us,p}/s_{uw,p}$

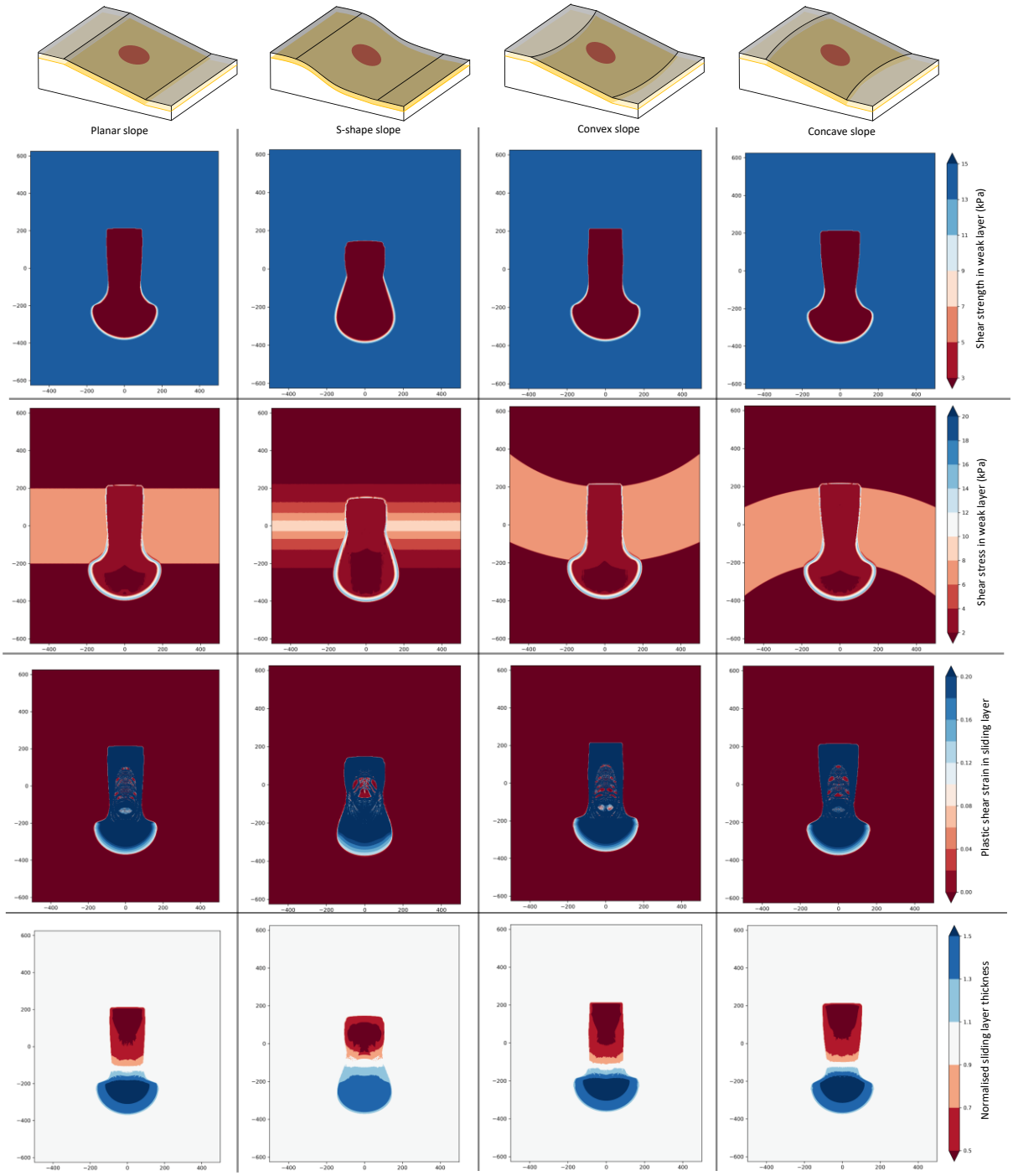

Figure 19 3D slope geometry effect on the ultimate slip surface growth and morphology of the mass transport deposit in translational landslides

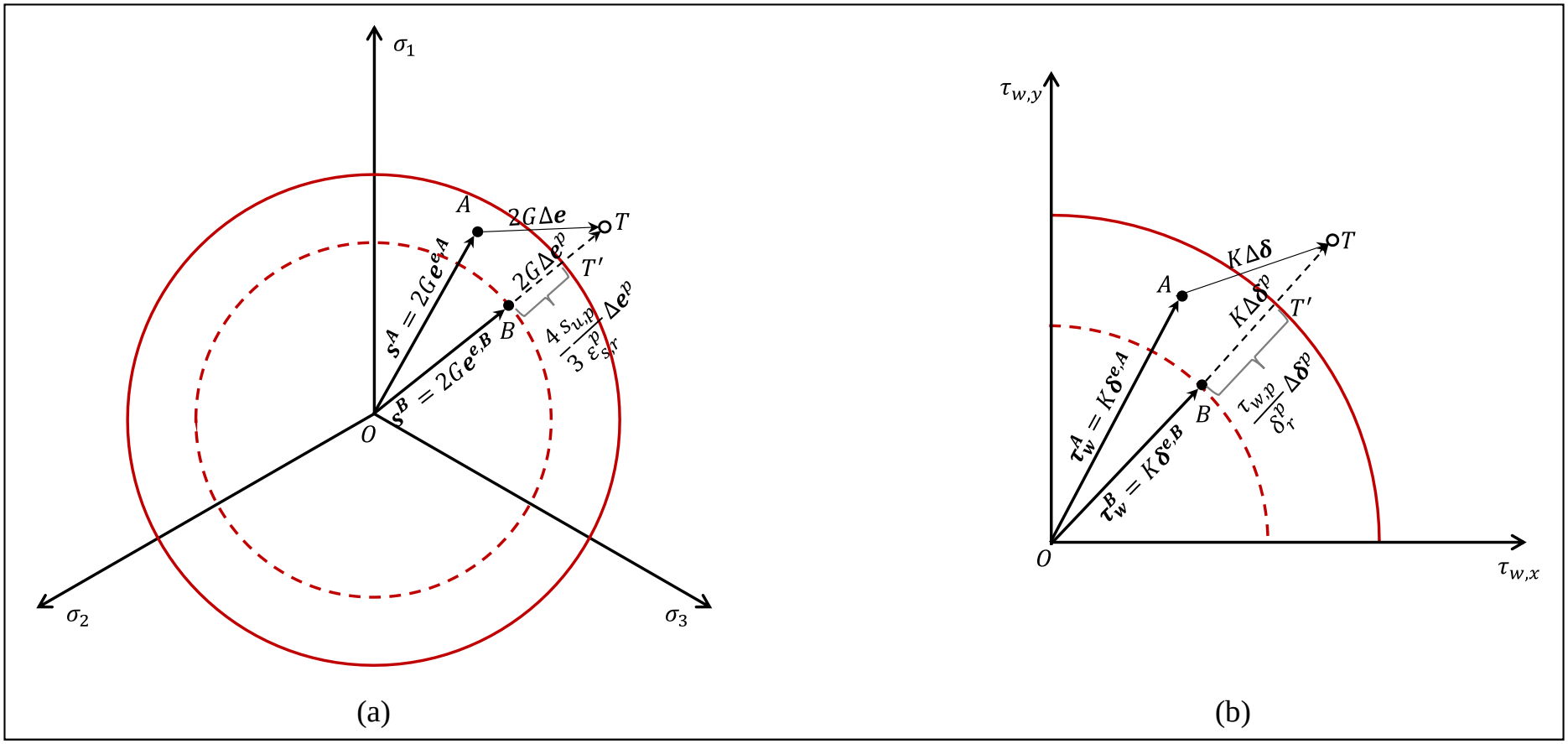

Figure A1 Constitutive models of soils in (a) sliding layer and (b) weak layer

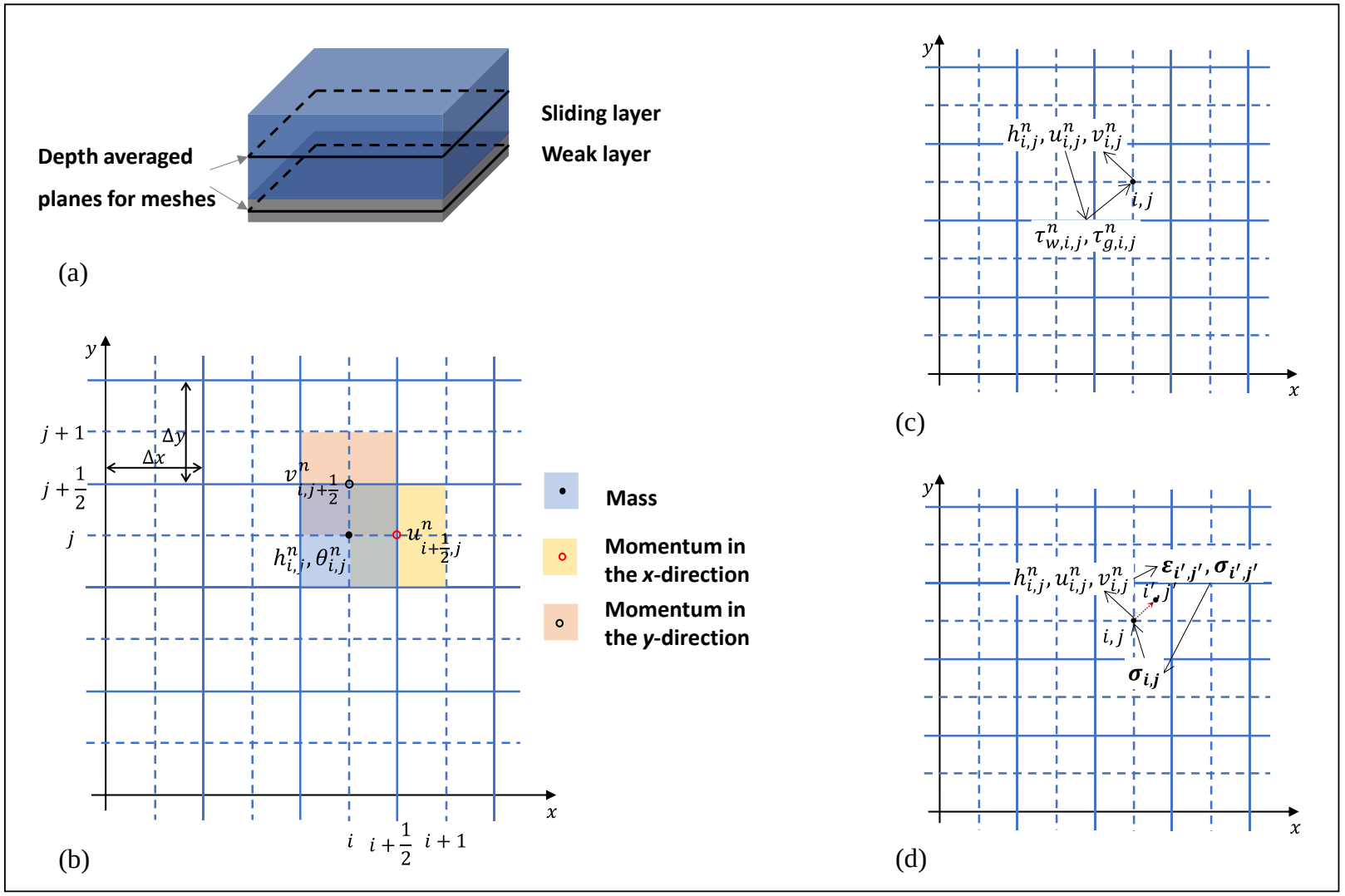

Figure A2 (a) Schematics of depth integrated model; (b) staggered mesh scheme; (c) update of properties for the fixed weak layer; and (d) update of properties for the movable sliding layer